

RESEARCH ACTIVITIES III Department of Electronic Structure

III-A Synthesis and Characterization of Exotic Molecule-Based Nano-Clusters with Transition Metals : Behavior as Single Domain Magnets

Molecule-based nanoclusters with transition metals are highly important in introducing electronic and magnetic functionalities in nanoelectronic devices. In view of electronic structure of metal- π conjugate systems, $M-C_2$ molecules, where $M = Fe, Co, Ni$ etc., are expected to generate $d-\pi^*$ interaction networks on cluster $(M-C_2)_n$ formation or on solidification. The ground state of $Co-C_2$ molecule is predicted to be 4B_1 with a symmetric triangular configuration where the $4s$ and d -orbital occupation numbers are far from integer, and the energy range of the upper sextets is only 5–6 kcal/mol (A.V. Arbuzniz and M. Hendriks, *Chem Phys. Lett.* **320**, 575 (2000)). Thus this high spin molecule should be very much suitable for making molecule-based nanocluster magnets. Here we report how we have generated molecule-based $(Co-C_2)_n$ magnets. The nano-size clusters isolated in amorphous carbon matrices are demonstrated to work as room-temperature single domain magnets.

III-A-1 Magnetic Behavior of Crude CoC_2 Solid Synthesized in Acetonitrile Solution

HINO, Kazuyuki¹; KOSUGI, Kentaroh; SEKIYA, Hiroshi¹; NISHI, Nobuyuki
(¹Kyushu Univ.)

CoC_2 molecules are synthesized from $CoCl_2$ and CaC_2 in acetonitrile or benzonitrile solution. The reaction scheme is expected as follows:



This reaction occurs on the surface of the CaC_2 particles in the solutions. Thus the structure of the solid products is not homogeneous. The infrared spectrum of the raw materials indicated that the commercial CaC_2 was heavily contaminated with $Ca(OH)_2$ and H_2O . The product solid was washed with water to convert CaC_2 to $Ca(OH)_2$ and C_2H_2 and the residual $CoCl_2$, $CaCl_2$ and $Ca(OH)_2$ were also removed by water. The color of the final product was greenish black. The infrared spectrum of the product exhibited the doublet band at 1375 and 1475 cm^{-1} that corresponds to the doublet band of CaC_2 at 1420 and 1500 cm^{-1} . The energy dispersed X-ray emission analysis indicated that the cobalt to carbon ratio changes from particle to particle in the range of 1.5 to 2.0. The particles containing higher oxygen concentration (due to water or OH contamination) exhibited lower ratios. The evolution of $(CoC_2)_n$ clusters in these particles is thought to be blocked by the inclusion of the hydroxide or water molecules. Figure 1 shows the temperature dependence of the magnetic susceptibility of the solid CoC_2 synthesized in acetonitrile. The CoC_2 solid produced in benzonitrile solution showed much larger susceptibility and the reason is ascribed to less water contamination in benzonitrile. The inserted graph in Figure 1 shows the magnetic hysteresis curve of the product in acetonitrile. The cohesive force of the CoC_2 solid produced in benzonitrile solution was 500 Oe at 1.8 K. Thus the $Co^{++}C_2^{-}$ salt compound becomes cluster

magnets at the temperatures lower than 4.5 K. The removal of the interstitial impurity species from the solid is expected to produce crystalline magnets that works at higher temperatures.

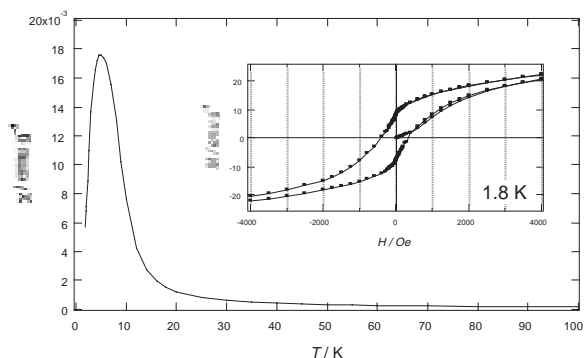


Figure 1. Temperature change of the magnetic susceptibility of CoC_2 solids synthesized from $CoCl_2$ and CaC_2 in acetonitrile solution.

III-A-2 Electron Microscope and EXAFS Study of Matrix Embedded $(Co-C_2)_n$ Nano-Cluster Magnets

NISHI, Nobuyuki; KOSUGI, Kentaroh; HINO, Kazuyuki¹; YOKOYAMA, Toshihiko; OKUNISHI, Eiji²
(¹Kyushu Univ.; ²JEOL Co. Ltd.)

$(Co-C_2)_n$ nanoparticles are synthesized from CH_2Cl_2 solution of $Co_4(CO)_{12}$ by heating up to 210 °C in a closed vessel. The cluster particles are embedded in amorphous carbon. Transmission electron microscope (TEM) observation of the particles provides a size distribution with an average size of 12 nm. Figure 1-a shows a TEM image of a relatively large nanocluster embedded in the matrix. Although most of the nanoparticles exhibited the single array of the lattice stripes (just like a single nanocrystals) as seen in the expanded image c, the upper part of this particle shows disor-

dered, thereby, three dimensional “step” structure around the border region between the upper and the middle parts (expanded image b). The image of the step area reminds us a structure similar to NaCl type crystals. The image of the matrix in the expanded view c shows an amorphous structure in contrast to the ordered structure of the particle. Figure 1-b displays the electron energy loss spectra of the nanoparticles (a) and the matrix (b) observed with an electron beam size of 2.5 nm. The bottom frame shows that the Co-L bands at 781 and 796 eV are seen for the nanoparticle but the matrix does not show any signals of Co component. The shape of the matrix C-K band is characteristic of amorphous carbon, while the spectral feature of the nanoparticle exhibits the enhanced π^* resonance at 285 eV and the low energy shift of the σ^* resonance, characteristic of unsaturated (sp or sp^2) carbon bonds. The intensity ratio of the C-K bands provides a ratio of cobalt to carbon to be 1 : 2. The ratio and the presence of the π^* resonance band indicates that the cluster is $(\text{Co}^{2+}\text{C}_2^{2-})_n$. The observed salt type structure image similar to that of a $\text{Ca}^{2+}\text{C}_2^{2-}$ crystal is in accord with this assignment. The radial structure function (RSF) obtained by Fourier transformation of extended X-ray absorption fine structure (EXAFS) provided the strongest Co–C peak at 2.08 Å and the two Co–Co peaks at 3.18 Å and 3.9(\pm 0.2) Å. These structural parameters are also in good agreement with the salt type structure for the $(\text{Co}^{2+}\text{C}_2^{2-})_n$ clusters, although the every Co and C_2 in the cluster is bonded with $d-\pi^*$ valence bond networks.

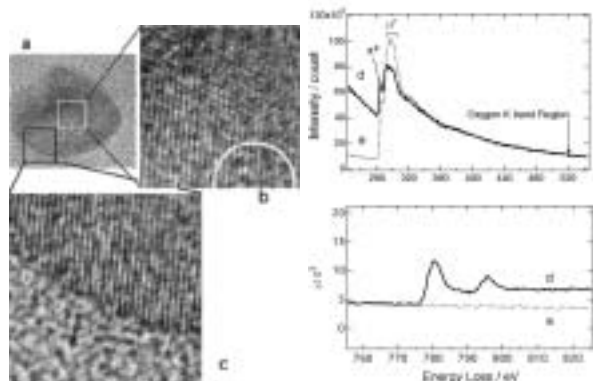


Figure 1. left: A TEM image of a relatively large particle in the matrix. The upper part was scraped off by the slicing knife of the microtome cutting machine exhibiting the disordered steps (image b). ($5 \times 5 \text{ nm}^2$) Image c shows the structural contrast of the nanoparticle with that of the amorphous carbon matrix. ($6 \times 6 \text{ nm}^2$)

Right: Electron energy loss spectra of the nanoparticle (of which image is shown on the left, spectrum d) and the matrix (spectrum e).

III-A-3 Magnetic Behavior of Matrix Embedded $(\text{Co}-\text{C}_2)_n$ Nano-Clusters as Single Domain Room-Temperature Magnets

KOSUGI, Kentaroh; HINO, Kazuyuki¹;
YOKOYAMA, Toshihiko; NISHI, Nobuyuki
(¹Kyushu Univ.)

Magnetic properties of the $(\text{Co}-\text{C}_2)_n$ nanoparticles embedded in the amorphous carbon matrix were mea-

sured with a SQUID magnetometer (Quantum Design MPMS-7S). Figure 1 shows the temperature change of the magnetic susceptibility under the zero-field cooling (ZFC) condition and the field cooling (FC) at 10 Oe external field. The susceptibility decreases with decreasing temperature from 300 K to 20 K at zero field suggesting that the particles are interacting and prone to align antiparallel to each other, while under the field cooling condition it increases with decreasing temperature. This means that the 10 Oe external field aligns the magnetic moments of the particles along the field direction. The two curves behaves just oppositely, and the average values are nearly temperature independent. The hysteresis shows that the saturation magnetization and the residual magnetization increases at lower temperatures while the cohesive force decreases at lower temperature. This behavior is in accord with the theoretical expectation for single domain magnets which exhibit cohesive force in inverse proportional to the saturation magnetization (S. Chikazumi, *Physics of ferromagnetism*, Shokabo, Vol II, 269 (1984)).

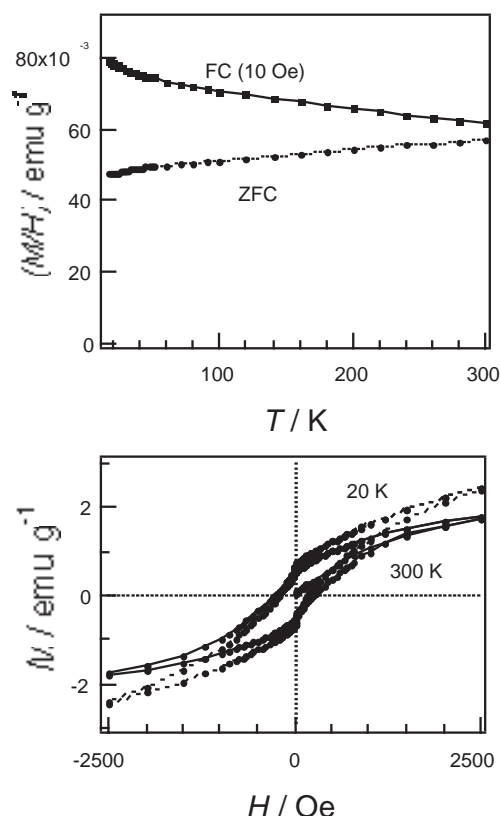


Figure 1. top: Temperature change of magnetic susceptibility of the matrix embedded $(\text{Co}-\text{C}_2)_n$ nano-clusters measured under the zero-field cooling condition (ZFC) and the field cooling (FC) condition. bottom: magnetic hysteresis curves at 300 K (solid curve) and 20 K (dotted curve).

III-A-4 Construction of Vacuum Apparatus for Mass-Resolved Spectroscopies of Non-Volatile Solid Samples

INOKUCHI, Yoshiya; HINO, Kazuyuki¹; NISHI, Nobuyuki
(¹Kyushu Univ.)

In order to apply mass-resolved spectroscopic methods to non-volatile samples, we need to vaporize them in a vacuum apparatus. In particular, for the samples prone to be damaged by water or oxygen, it is necessary to introduce them into the vacuum apparatus without being exposed by the air. Recently, we have constructed a new apparatus for mass-resolved spectroscopies of non-volatile (and non-metallic) solid samples. Figure 1 shows a schematic diagram of the apparatus. It consists of a liquid beam source, a titanium rotating drum, and a time-of-flight mass spectrometer. Non-volatile samples are dissolved in some volatile solvents. The solutions are injected through a modified injector needle into the vacuum chamber as a liquid beam. The surface of the rotating titanium drum is located at 5 mm away from the exit of the needle. The solvent is vaporized, and only the solute species are fixed on the drum. The solid sample on the drum is laser-desorped by the third harmonics of a Nd:YAG laser (355 nm) introduced through a hole between a sample chamber and a main chamber. The gaseous sample is ionized by three types of ionization technique: matrix-assisted laser desorption-ionization (MALDI), electron impact (EI), and resonance-enhanced multiphoton ionization (REMPI). The produced ions are mass-analyzed by the time-of-flight mass spectrometer. Since the non-volatile samples are directly introduced into the spectrometer as solutions and fixed on

the drum, the samples does not contact with the air. We can obtain excitation spectra of the samples by scanning the wavelength of the ionization laser. Photodissociation spectra of the sample ions can be measured by the introduction of a dissociation laser into the drift region of the spectrometer.

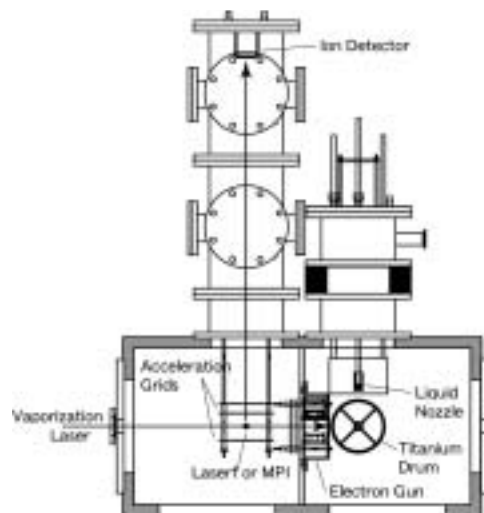


Figure 1. Schematic diagram of a time-of-flight mass spectrometer for solid samples.

III-B States of Neutral and Ionic Molecular Associates in Solutions

States of molecular associates particularly in aqueous solutions are of great importance in understanding the role of molecules in living organisms. We found that any ideally mixed state cannot be seen in protic-protic mixtures such as water-alcohol, water-acetic acid, and alcohol-acetic acid systems on the molecular level at solute molar fractions (χ_A) higher than 0.001. In such a system, solute-solute association is highly favored resulting in microscopic phase separation. Here we demonstrate that aprotic solvent such as acetonitrile can produce ideally mixed state(s) for acetic acid.

III-B-1 States of Molecular Associates in Binary Mixtures of Acetic Acid with Protic and Aprotic Polar Solvents: A Raman Spectroscopic Study

NAKABAYASHI, Takakazu; NISHI, Nobuyuki

[*J. Phys. Chem. A* **106**, 3491 (2002)]

The local structure of acetic acid in protic and aprotic polar solvents have been studied by Raman spectroscopy and ab initio calculations with the self-consistent reaction field (SCRf) method. As acetic acid is diluted in water, the C=O stretching Raman band of acetic acid becomes broader and shows a higher wavenumber shift from 1666 to 1710 cm^{-1} , which arise from the generation of acetic acid microphases. In the region of $0.001 \leq \chi_A$ (acetic acid mole fraction) ≤ 0.2 , both the peak position and the bandwidth of the C=O band are hardly changed, indicating that the acetic acid microphases exist even in the diluted solution at $\chi_A = 0.001$.

In alcohols (methanol, 1-butanol, and 1-hexanol), the spectral changes in the C=O stretching band with the dilution are almost the same as those observed in water, suggesting that the same acetic acid microphases are formed in the alcohol solutions at $\chi_A \geq 0.001$. In acetonitrile, however, the spectral changes are apparently different from those in the protic solvents: two higher wavenumber C=O bands at 1725 and 1754 cm^{-1} appear in the region of $0.001 \leq \chi_A \leq 0.3$. From the ab initio SCRf calculations, we assign the 1725 and 1754 cm^{-1} bands to the cyclic dimer consisting of acetic acid and acetonitrile monomers and to the noncomplexed acetic acid monomer, respectively. Such two bands are also observed in other nitriles and ethers, suggesting that the monomeric molecules are preferentially formed in aprotic polar solvents. From these results, it is concluded that binary solution of acetic acid and the protic solvent do not get homogeneously mixed even in the low acid concentration region of $\chi_A \geq 0.001$, while homogeneously mixed states at molecular levels occur

in the binary solutions of acetic acid and the aprotic polar solvents when the acetic acid mole fraction is small.

III-C Ultrafast Dynamics and Scanning Tunneling Microscopy

We have constructed a low temperature scanning tunneling microscope system combined with an ultrafast light sources in addition to the femtosecond time-resolved ionization detected spectrometer.

III-C-1 Construction of an Apparatus for Direct Observation of Reactions Induced by Ultrafast Laser Pulses Using a Low Temperature STM

OHSHIMO, Kejiro; NAKABAYASHI, Takakazu; WATANABE, Kazuo¹; NAGATA, Takashi¹; NISHI, Nobuyuki
(¹Univ. Tokyo)

Recent advances in laser technology have led to the development of ultrafast spectroscopic techniques that enable us to examine the dynamics of chemical reactions in the femto to picosecond time range. The next stage is to perform the real-space and high-resolution imaging of ultrafast chemical reactions. The ability to view molecular structural changes on an atomic scale in real time promises great progress in many fields of chemistry and physics. In the present study, we have constructed an apparatus for the visualization of photochemical reactions at surfaces by using a low-temperature UHV STM and a picosecond pulse laser system. Experimental arrangement is schematically depicted in Figure 1. The constructed system has two helium cooled STM cryostats, one of which operates to 8 K and has two optical windows for irradiation of laser beams. The angle of incidence is 45° with respect to the STM-tip axis. Optical illumination is provided by two independently tunable picosecond OPA systems. By using frequency mixings, we have obtained the tuning of light between 189 and 11200 nm with microjoule pulse energy and 4 ps pulse duration. Picosecond pump-probe experiments can be carried out with an optical delay stage. The other STM is constructed for low temperature STS studies. A sample in this cryostat can be controlled at any temperature between 4 K and 50 K and kept at 4 K for at least 24 hours without refilling He liquid. A sputtering and annealing system in a preparation chamber obtains a clean flat surface of a substrate. A molecular beam doser is equipped for the adsorption of target molecules onto a substrate. A pulse injection system with a high-speed solenoid valve is also installed for the deposition of nanoparticles and biomolecules. Both the STM cryostats have been confirmed to perform atomic resolution on topograph images of Si(111) surfaces at liquid helium temperatures. By using the former STM cryostat, we have observed Pd clusters with ≈ 6 nm diameters on Au(111) surfaces.

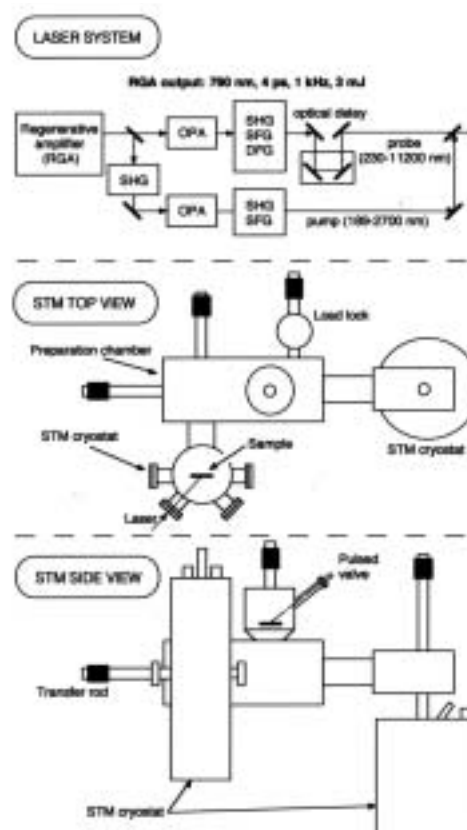


Figure 1. Schematic drawing of the experimental setup.

III-C-2 Construction of a Femtosecond Time-Resolved Ionization Detected Spectrometer

OKABE, Chie¹; NAKABAYASHI, Takakazu; INOKUCHI, Yoshiya; SEKIYA, Hiroshi¹; NISHI, Nobuyuki
(¹Kyushu Univ.)

A time-of-flight mass spectrometer combined with a supersonic molecular beam and a femtosecond laser system has been constructed to observe the ultrafast reaction dynamics of molecules and clusters in the gas phase. The femtosecond laser system consists of a mode-locked Ti:sapphire oscillator with a tunable wavelength from 720 to 850 nm, a regenerative amplifier pumped by a frequency-doubled Nd:YLF laser at 1 kHz, and an optical parametric amplifier (OPA) system. The output from the OPA is tuned between 300 and 10000 nm by mixing techniques and is used for pumping sample molecules to the photoexcited states. A portion

of the output from the regenerative amplifier is frequency doubled (or tripled) and used as a probe beam for ionizing transient molecules generated by the pump beam. After passing through fixed (for the pump beam) and variable (for the probe beam) optical delay lines, the pump and probe beams are superimposed by a dichroic mirror, and focused into a vacuum chamber with an $f = 350$ mm focal lens. Gas mixture of sample molecules and helium is expanded into the vacuum chamber through a pulsed nozzle with a 0.80 mm orifice diameter and a 300 microsec pulse duration. The laser beams merge with the molecular beam and ionize the sample molecules in the acceleration region. The product ions are mass analyzed in the time-of-flight mass spectrometer and are detected using a microsphere plate detector. The ion signals are collected at a 10 Hz repetition rate synchronized with the opening of the pulsed nozzle and are fed into a digital storage oscilloscope. The oscilloscope and the optical delay stage are controlled by a microcomputer through a GPIB interface. The instrumental response function is determined by the pump-probe ionization experiments on pyrazine and benzene that are known to exhibit an instrument-limited rise. It is estimated to be a Gaussian function with a full width at half maximum of 230 fs. Time-resolved multiphoton ionization intensities of N-salicylideneaniline and diarylethene derivatives have been observed by using this spectrometer.

III-C-3 Picosecond Time-Resolved Raman Studies on the Photochromic Reactions of Diarylethenes

OKABE, Chie¹; NAKABAYASHI, Takakazu;
NISHI, Nobuyuki; FUKAMINATO, Tuyoshi¹;
KAWAI, Tsuyoshi¹; IRIE, Masahiro¹; SEKIYA,
Hiroshi¹
(¹Kyushu Univ.)

Diarylethenes are promising photochromic compounds for optoelectronic applications because of their fatigue-resistant and thermally irreversible properties. The open forms of diarylethenes are mostly colorless and turn to the closed forms by UV irradiation. The generated closed forms are thermally stable and exhibit absorption spectra in the visible region. Upon irradiation of visible light, the closed forms revert back to the original open forms. In the present study, we have first measured picosecond time-resolved Stokes and anti-Stokes Raman spectra of diarylethenes in solutions, in order to obtain the rates and mechanisms of these photochromic reactions. We have used 1,2-bis(2,5-dimethyl-

3-thienyl)perfluorocyclopentene for the ring-closure reaction, and 1,2-bis(3,4-dimethyl-5-phenyl-2-thienyl)perfluorocyclopentene for the ring-opening reaction. Two common features of the ring-closure and ring-opening reactions are found: the photochromic reactions proceed in the time scale less than 4 ps and the vibrationally excited molecules in the ground electronic (S_0) state are generated as the intermediate state. Figure 1 shows the time-resolved anti-Stokes Raman spectra of 1,2-bis(3,4-dimethyl-5-phenyl-2-thienyl)perfluorocyclopentene. The observed two anti-Stokes Raman bands at 1545 and 1599 cm^{-1} are assignable to the C=C stretching modes of the thiophene and cyclopentene moiety of the generated S_0 open forms, respectively. The intensity of the cyclopentene moiety relative to that of the thiophene moiety becomes smaller with the delay time, indicating part of the excess energy generated via the ring-opening reaction is localized on the C=C stretching mode of the cyclopentene moiety. This means that the C=C stretching mode of the cyclopentene moiety is one of the promoting or the accepting modes in the ring-opening reaction.

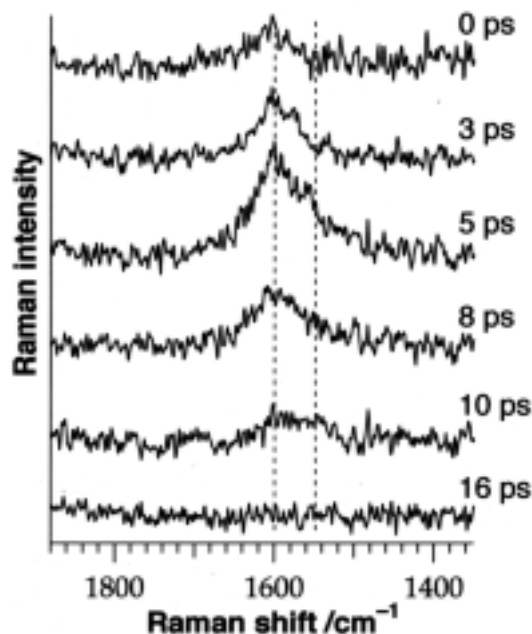


Figure 1. Picosecond time-resolved anti-Stokes Raman spectra of 1,2-bis(3,4-dimethyl-5-phenyl-2-thienyl)perfluorocyclopentene in acetonitrile. Pump, 480 nm; probe, 395 nm. The delay time is given on the right side of each spectrum.

III-D Spectroscopic and Dynamical Studies of Molecular Cluster Ions

Electron deficiency of molecular cluster cations can attract electron rich groups or atoms exhibiting charge transfer or charge resonance interaction in the clusters. This causes dynamical structural change such as proton transfer or ion-core switching in hot cluster ions or clusters in solution.

III-D-1 Intermolecular Interactions in Aniline/Benzene Hetero-Trimer and Aniline Homo-Trimer Ions

OHASHI, Kazuhiko¹; INOKUCHI, Yoshiya; NISHI, Nobuyuki; SEKIYA, Hiroshi¹
(¹Kyushu Univ.)

[*Chem. Phys. Lett.* **357**, 223 (2002)]

The charge distribution and binding features of aniline/benzene hetero-trimer and aniline homo-trimer ions are investigated by vibrational spectroscopy and by near-infrared photodissociation and spontaneous unimolecular dissociation of mass-selected cluster ions. The absence of the charge resonance absorption indicates the charge localization in the trimer ions. Substantial red-shifts and enhanced intensities of the NH-stretching transitions suggest large intermolecular perturbations. The trimer ions are stabilized by the hydrogen-bonding interaction through the NH₂ group of the charged aniline with the neutral molecules rather than the charge-delocalization interaction among the component molecules.

III-D-2 Infrared Photodissociation Spectroscopy of Protonated Formic Acid-Water Binary Clusters, H⁺·(HCOOH)_n·H₂O (*n* = 1–5). Spectroscopic Study of Ion Core Switch Model and Magic Number

INOKUCHI, Yoshiya; NISHI, Nobuyuki

[*J. Phys. Chem. A* **106**, 4529 (2002)]

Infrared spectra of protonated formic acid-water binary clusters, H⁺·(HCOOH)_n·H₂O (*n* = 1–5), are investigated by infrared photodissociation spectroscopy and ab initio molecular orbital calculations. The asymmetric OH stretching vibration of water is observed in the infrared photodissociation spectra of the clusters with *n* = 1–3; it disappears in the spectra of the *n* = 4 and 5 clusters. On detailed comparison of the observed infrared spectra with calculated ones, the most stable geometric structures are obtained for the *n* = 1–5 clusters. These results suggest that the clusters switch the ion cores from HCOOH₂⁺ for *n* = 1–3 to H₃O⁺ for *n* = 4 and 5. The *n* = 5 cluster has a cyclic-type structure; the H₃O⁺ ion core is fully surrounded and stabilized by five formic acid molecules. This characteristic nature produces a magic number of the *n* = 5 cluster.

III-D-3 Infrared Photodissociation Spectroscopy of Aniline⁺–(Water)_{1,2} and Aniline⁺–(Methanol)_{1,2}

HONKAWA, Yoshiki¹; INOKUCHI, Yoshiya; OHASHI, Kazuhiko¹; NISHI, Nobuyuki; SEKIYA, Hiroshi¹
(¹Kyushu Univ.)

[*Chem. Phys. Lett.* **358**, 419 (2002)]

Infrared photodissociation spectra of the aniline ion

solvated by water and methanol molecules are measured in the 2600–3800 cm⁻¹ region. Substantially red-shifted and broadened transition is distinctly observed at 3105 and 2915 cm⁻¹ for aniline⁺–(H₂O)₁ and aniline⁺–(CH₃OH)₁, respectively, and assigned to the stretching vibration of the hydrogen-bonded NH oscillator of the aniline⁺ moiety. The spectra of aniline⁺–(H₂O)₂ and aniline⁺–(CH₃OH)₂ demonstrate a large perturbation to both of the NH oscillators, indicating that each NH bond is bound to a solvent molecule in the most stable structure.

III-D-4 Intracluster Proton Transfer in Aniline–Amine Complex Ions

INOKUCHI, Yoshiya; OHASHI, Kazuhiko¹; HONKAWA, Yoshiki¹; SEKIYA, Hiroshi¹; NISHI, Nobuyuki
(¹Kyushu Univ.)

[*Chem. Phys. Lett.* **359**, 283 (2002)]

The intracluster proton transfer in aniline–amine complex ions is investigated by infrared photodissociation spectroscopy and density functional theory calculations. The proton acceptors include ammonia, methylamine, dimethylamine and trimethylamine in ascending order of proton affinity. The spectra of (aniline–ammonia)⁺ and (aniline–methylamine)⁺ demonstrate the persistence of the aniline ion unit in the complexes. For (aniline–dimethylamine)⁺ and (aniline–trimethylamine)⁺, the spectra imply the transformation to the anilino radical (C₆H₅NH) unit, suggesting the occurrence of the proton transfer.

III-D-5 LIF and IR Dip Spectra of Jet-Cooled *p*-Aminophenol–*M* (*M* = CO, N₂): Hydrogen-Bonded or van der Waals-Bonded Structure?

MORI, Hirotoshi¹; KUGISAKI, Hitomi¹; INOKUCHI, Yoshiya; NISHI, Nobuyuki; MIYOSHI, Eisaku¹; SAKOTA, Kenji¹; OHASHI, Kazuhiko¹; SEKIYA, Hiroshi¹
(¹Kyushu Univ.)

[*J. Phys. Chem. A* **106**, 4886 (2002)]

Intermolecular interaction and stable structures of the *p*-aminophenol–*M* (*M* = CO, N₂) 1:1 complexes have been studied by measuring the *S*₁–*S*₀ fluorescence excitation spectra and the IR dip spectra in the OH and NH stretch region. We also have performed ab initio calculations to obtain stable structures and calculated infrared spectra of the complexes. The *S*₁–*S*₀ electronic origin of the CO complex is 141 cm⁻¹ red shifted from that of the monomer. This shift is smaller than that of the N₂ complex (153 cm⁻¹), although the molecular polarizability of CO is larger than that of N₂. The IR dip spectrum of the CO complex shows that the OH stretching frequency is 26 cm⁻¹ lower than that of the monomer. On the other hand, the N₂ complex displays no shift. We conclude that the CO molecule is bonded to the OH group *via* a hydrogen bond in *p*-aminophenol–CO, whereas the N₂ molecule is van der Waals-

bonded to the π cloud of the aromatic ring in *p*-aminophenol–N₂.

III-D-6 Structure and Intermolecular Hydrogen Bond of Jet-Cooled *p*-Aminophenol–(H₂O)₁ Studied by Electronic and IR-Dip Spectroscopy and Density Functional Theory Calculations

MORI, Hirotoshi¹; KUGISAKI, Hitomi¹;
INOKUCHI, Yoshiya; NISHI, Nobuyuki;
MIYOSHI, Eisaku¹; SAKOTA, Kenji¹; OHASHI,
Kazuhiko¹; SEKIYA, Hiroshi¹
(¹Kyushu Univ.)

[*Chem. Phys.* **277**, 105 (2002)]

The structure and hydrogen bonding interaction in jet-cooled *p*-aminophenol–H₂O 1:1 complex have been studied by measuring the fluorescence excitation, dispersed fluorescence, and IR-dip spectra. In the electronic spectrum we identified only one isomer, where the oxygen atom of water is bonded to the hydroxy proton of *p*-aminophenol. Four stable isomers are obtained by ab initio calculations at the MP2/6-31G(d) level, while density functional theory calculations provide four or three isomers depending on the basis sets. It has been shown that theoretical IR spectra with small basis sets are not in agreement with the experimental IR spectrum. The experimental IR spectrum has been well reproduced by the B3LYP/6-311+G(d,p) calculations, showing that diffuse functions are necessary to describe the intermolecular hydrogen bond in *p*-aminophenol–H₂O. The vibronic levels in the *S*₁ state of *p*-aminophenol–H₂O have been assigned with the aid of the dispersed fluorescence spectra. The formation of the intermolecular hydrogen bond substantially reduces the frequency of the amino inversion mode in the *S*₁ state due to nonlocal character of this mode.

III-D-7 Positive Charge Distribution in (Benzene)₁(toluene)₂⁺ and (Benzene)₂(toluene)₁⁺ Studied by Photodissociation Spectroscopy

INOKUCHI, Yoshiya; OHASHI, Kazuhiko¹;
SEKIYA, Hiroshi¹; NISHI, Nobuyuki
(¹Kyushu Univ.)

[*J. Chem. Phys.* in press]

The positive charge distribution in benzene–toluene hetero-trimer ions is investigated by photodissociation spectroscopy in the near-infrared (6000–14000 cm⁻¹) and infrared (2800–3150 cm⁻¹) regions. The electronic spectra of (benzene)₁(toluene)₂⁺ and (benzene)₂(toluene)₁⁺ in the near-infrared region display a strong band at 9430 and 8330 cm⁻¹, respectively. These bands are ascribed to the charge resonance band; the positive charge is not localized on a single molecule. The vibrational spectrum of (benzene)₁(toluene-*d*₈)₂⁺ shows three distinct bands at 3054, 3084, and 3108 cm⁻¹; these bands are assigned to the CH stretching vibrations of the benzene moiety. The similarity of the spectral features to those of the neutral benzene monomer suggests that

the benzene molecule in the (benzene)₁(toluene)₂⁺ ion has a neutral character. The positive charge is localized on the toluene dimer unit with a structure written as (toluene)₂⁺⋯(benzene)₁. The vibrational spectrum of (benzene)₂(toluene)₁⁺ bears a resemblance to that of (benzene)₂⁺. The vibrational spectrum of (benzene-*d*₆)₂(toluene)₁⁺ shows dissimilar features to the spectrum of the neutral toluene monomer, suggesting that a certain amount of the positive charge is carried by the toluene moiety. These results are explained by the charge resonance interaction between (benzene)₂ and (toluene)₁. A simple perturbation theory is applied for determining the positive charge distribution in (benzene)₂(toluene)₁⁺. The probability of finding the charge on the (benzene)₂ and (toluene)₁ moieties is analyzed to be 58 and 42 %, respectively.

III-D-8 Infrared Photodissociation Spectroscopy of [Aniline–(Water)_{*n*}]⁺ (*n* = 1–8)

INOKUCHI, Yoshiya; HONKAWA, Yoshiki¹;
OHASHI, Kazuhiko¹; SEKIYA, Hiroshi¹; NISHI,
Nobuyuki
(¹Kyushu Univ.)

Infrared photodissociation spectra of [aniline–(H₂O)_{*n*}]⁺ (*n* = 1–8) are measured in the 2700–3800 cm⁻¹ region. The spectra are interpreted with the aid of density functional calculations. A substantially red-shifted and broadened transition is distinctly observed at 3105 cm⁻¹ for the *n* = 1 ion, and assigned to the stretching vibration of the hydrogen-bonded NH oscillator of the aniline⁺ moiety. The spectrum of the *n* = 2 ion demonstrates a large perturbation to both of the NH oscillators, indicating that each NH bond is bound to a water molecule in the most stable structure. For the *n* = 3 ion, three broad bands exist at 3070, 3230, and 3420 cm⁻¹, and there are two maxima and a weak hump at 3637, 3723, and 3696 cm⁻¹. The calculated spectrum of the 2-1 branch structure resembles the observed one very well. For the *n* = 4 ion, there exist three strong bands at 2960, 3100, and 3430 cm⁻¹, and a very weak one at 3550 cm⁻¹. The observed spectrum in the 3600–3800 cm⁻¹ region is decomposed into four bands at 3640, 3698, 3710, and 3734 cm⁻¹. These bands are originated from the 2-2 branch isomer except for the 3550 and 3710 cm⁻¹ bands. These two bands are due to the other isomer that has the five-membered ring. A characteristic transition in the observed spectrum of the *n* = 5 ion is the 3684 cm⁻¹ band, which hardly emerges in the spectra of *n* = 1–4. This band is assigned to the free OH stretching vibration of the three-coordinated (double-acceptor–single-donor) H₂O, indicating the ring structure. The *n* = 5 ion has the five-membered ring structure with the fifth water molecule bound to the terminal (double-acceptor) H₂O. The observed spectra of the *n* = 6–8 ions show features quite different from those of *n* = 1–5; a very strong and broad band emerges around 3400 cm⁻¹. It is suggested that the *n* = 6–8 ions have the proton transfer form with some ring structure.

III-E Spectroscopy and Dynamics of Vibrationally Excited Molecules and Clusters

This research group is studying structure and dynamics of molecules and clusters by two-color double resonance spectroscopy. New spectroscopic methods will also be developed to observe the higher vibrational state under collision-free condition.

A molecular cluster is a microscopic system of solution and/or crystal, and is thought to provide detailed information on relaxation and reaction dynamics in condensed phase. However the previous studies are concentrated to stable clusters which has no reaction pathway after photo-excitation. Consequently, spectroscopic information which concerns the reaction mechanism has not been obtained sufficiently. In this research project started from 2000, we will apply various laser spectroscopies to the reactive clusters to reveal detailed mechanism of intracuster reaction.

For the study of the ground state, the structure of the cluster can be determined by the combination of the IR dip spectroscopy and *ab initio* MO calculations.¹⁾ The IR dip spectroscopy is a kind of IR-UV double resonance spectroscopy which provides the spectrum which corresponds to the infrared absorption spectrum of the cluster (see Figure 1). A tunable IR laser is introduced to the clusters and is scanned its frequency over the fundamental vibrational region (typically 2400 ~ 4000 cm^{-1}). Then a tunable UV laser, of which the frequency is fixed to the S_1 origin of a specific cluster, is introduced and resonant enhanced multiphoton ionization signal *via* S_1 is monitored. When the IR laser is resonant to a vibrational level of the cluster, the ion signal decreases much because of loss of the population in the vibrational ground state. Thus, the IR absorption spectrum of the cluster can be measured by this depletion spectroscopy. The same spectrum can be obtained when the fluorescence intensity from S_1 is monitored instead of the ion current.

The IR spectrum in the excited state S_1 can also be measured by the depletion spectroscopy, when the UV laser is introduced before the IR laser (the UV-IR fluorescence dip spectroscopy; see Figure 2). The molecule is excited to S_1 by the UV laser, and the fluorescence intensity is monitored as well as the IR dip spectroscopy for S_0 . Then the S_1 molecules are further excited to the vibrationally excited level in S_1 by the IR laser. In general, the fluorescence quantum yield decreases in the higher vibronic level. Thus, the total fluorescence intensity decreases when the IR laser frequency is resonant to the vibrational level in S_1 .

Similarly, the IR spectrum of the ionic cluster can be measured by the depletion spectroscopy (mass-selected ion dip spectroscopy; see Figure 3). The ionic cluster can be prepared by the multiphoton ionization *via* S_1 , and the ion current due to the cation cluster of the specific size can be measured through a mass-filter. When the ionic cluster is vibrationally excited by the IR laser, the cluster is dissociated by the vibrational predissociation. Therefore, the IR transition can be measured by the decrease of the parent cluster. The same spectrum can be obtained by monitoring the enhancement of fragments (mass-selected multiphoton dissociation spectroscopy). In addition to these "dip" spectroscopies, the nonresonant ionization detected IR spectroscopy²⁾ and the PFI-ZEKE photoelectron spectroscopy³⁾ are also important tool to obtain the spectral information in the cation and the overtone states. Based on these spectroscopic techniques, we have measured the IR spectra of solvated clusters,⁴⁾ such as phenol/ammonia,⁵⁾ naphthol/alcohol,⁶⁾ carbazole/water⁷⁾ and 7-azaindole dimers,⁸⁾ and have discussed the relation among geometrical structure, electronic state and intracuster reactions.

From 2001, we have been developing the new ultrafast time-resolved IR spectroscopy for the reactive clusters. The pico second time-resolved vibrational spectroscopy is one of the ideal way to reveal the reaction mechanism directly. Here, we will demonstrate its usefulness by applying the hydrogen transfer reaction in photoexcited PhOH-

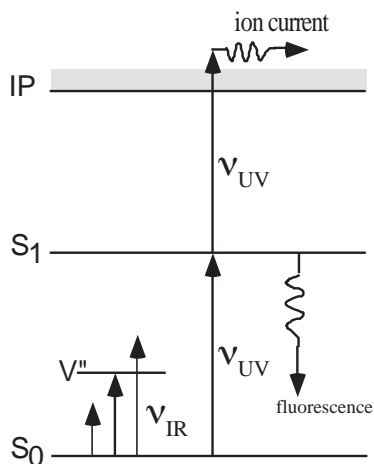


Figure 1. Principle of the IR Dip Spectroscopy. The IR transition in the ground state cluster can be measured.

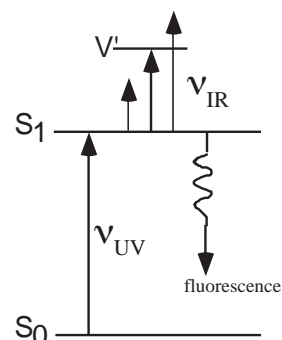


Figure 2. Principle of the UV-IR Fluorescence Dip Spectroscopy. The IR transition of the cluster in the S_1 state can be obtained.

(NH_3) $_n$ cluster.⁹⁾ Figure 4 shows the principle of the picosecond time-resolved UV-IR-UV ion dip spectroscopy. The reactive cluster ($\text{PhOH}(\text{NH}_3)_n$ in present case) is excited to S_1 by a picosecond UV laser ν_{UV} and the photochemical reaction (hydrogen transfer) is triggered. The final reaction product, *i. e.* (NH_3) $_{n-1}\text{NH}_4$, is ionized by a nanosecond UV laser ν_{ION} which is irradiated after 100 ns from ν_{UV} and the population of the reaction product is monitored as a mass peak of (NH_3) $_{n-1}\text{NH}_4^+$. A picosecond tunable IR laser ν_{IR} is irradiated after t ps from ν_{UV} and is scanned over vibrational region. If ν_{IR} is resonant to vibrational levels of the transient species, the population of the final reaction product decreases due to the vibrational predissociation of the transient species. Therefore, the vibrational transitions of the transient species at t ps can be observed as decrease of ion current of the final reaction product.

Time resolved UV-IR-UV ion dip spectra of phenol-(NH_3) $_3$ are shown in Figure 5. The numbers in the left hand sides of each spectrum indicate the delay time from ν_{UV} to ν_{IR} . Here the spectrum at -20 ns corresponds to the IR spectrum of $\text{PhOH}(\text{NH}_3)_3$ in S_0 , in which the sharp bands at 3400 cm^{-1} , the broad bands at $\sim 3200\text{ cm}^{-1}$ and the very broad background are assigned to the degenerated antisymmetric stretch vibration ν_3 in NH_3 , the totally symmetric stretch vibration ν_1 in NH_3 and the OH stretch vibration ν_{OH} in phenol, respectively. The spectrum at $+180$ ns shows the vibrational transitions of the final reaction product *via* S_1 , *i. e.* (NH_3) $_2\text{NH}_4$, and 1) two intense bands at 3180 cm^{-1} and 3250 cm^{-1} and 2) a broad band at $2700 \sim 3100\text{ cm}^{-1}$ which have been assigned to

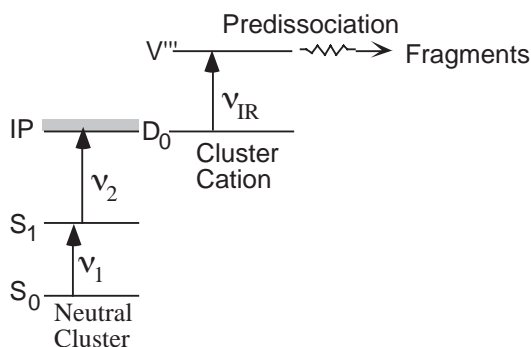


Figure 3. Principle of the mass-selected IR Ion Dip Spectroscopy. The IR transition of the cluster cation can be measured by the depletion of the parent cluster cation. The same spectrum can be measured by monitoring the enhancement of the fragments produced by the IR predissociation.

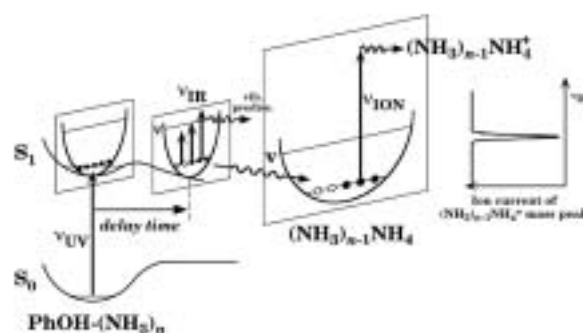
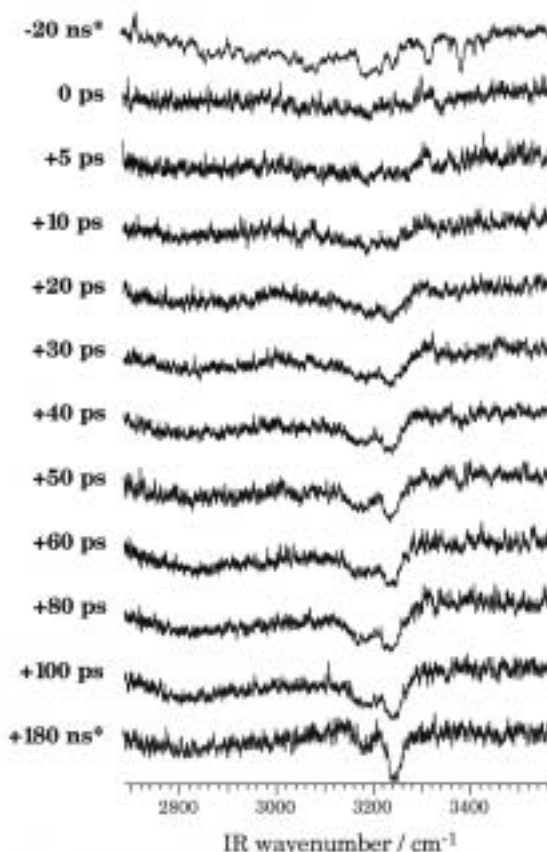


Figure 4. Principle of picosecond time-resolved UV-IR-UV ion dip spectroscopy. Potential curves of S_0 and S_1 are schematically drawn along O-H stretch coordinate. Potential curves in different sections on the S_1 O-H stretch coordinate are drawn along arbitrary N-H stretch coordinates.

Figure 5. Picosecond time-resolved UV-IR-UV ion dip spectra of the transient species from the electronically excited $\text{PhOH}(\text{NH}_3)_3$ which was observed by fixing ν_{UV} to the low vibronic band in the S_1 state of $\text{PhOH}(\text{NH}_3)_3$ (281.49 nm) and monitoring (NH_3) $_2\text{NH}_4^+$ due to ν_{ION} (355 nm). Times indicated at the left side of each spectrum mean the delay times between ν_{UV} and ν_{IR} . The spectra whose delay times are -20 ns and $+180\text{ ns}$ (indicated by *) are obtained by nanosecond laser system, which have been reported in the previous paper.⁵⁾



vibrational transitions concerned with NH_4 .

One can see that the vibrational bands rise with increasing delay time. The spectral feature at +100 ps is already similar to that of the final reaction product (+180 ns). Here, the intense band at 3250 cm^{-1} rises slower than the band at 3180 cm^{-1} . The relative intensities of the two bands become comparable at 40 ps, thereafter, the higher band at 3250 cm^{-1} clearly grows further. Thus, the rising time constant of the band at 3250 cm^{-1} is apparently different from that of the 3180 cm^{-1} -band. This remarkable difference between the two intense bands suggests that each vibrational transition is derived from different species. The existence of two transient species are naturally interpreted by considering the isomers of $(\text{NH}_3)_2\text{NH}_4$; the most stable $\text{NH}_3\text{-NH}_4\text{-NH}_3$ and the meta-stable $\text{NH}_4\text{-NH}_3\text{-NH}_3$. The co-existence of isomers is strongly supported by *ab initio* calculations.

As described above, we have successfully measured the picosecond time resolved IR spectra of the transient species for the ESHT of $\text{PhOH-(NH}_3)_3$ for the first time. It proves that the picosecond UV-IR-UV ion dip spectroscopy is a powerful tool to explore the dynamics of the intracluster reaction.

References

- 1) R. Yoshino *et al.*, *J. Phys. Chem. A* **102**, 6227 (1998).
- 2) T. Omi *et al.*, *Chem. Phys. Lett.* **252**, 287 (1996); S. Ishiuchi *et al.*, *Chem. Phys. Lett.* **283**, 243 (1998).
- 3) K. Takazawa *et al.*, *Chem. Phys. Lett.* **189**, 592 (1992); K. Müller-Dethlefs *et al.*, *Z. Naturforsch. Teil A* **39**, 1089 (1984); K. Müller-Dethlefs and M. C. R. Cockett, "Zero Kinetic Energy (ZEKE) Photoelectron Spectroscopy," Chapter 7, "Nonlinear Spectroscopy for Molecular Structure Determination," R. W. Field *et al.*, Eds., (Blackwell Science, Oxford, 1998), and references therein.; E. W. Schlag, "ZEKE Spectroscopy" (Cambridge University Press, Cambridge, 1998), and references therein.
- 4) K. Suzuki, Y. Emura, S. Ishiuchi and M. Fujii, *J. Electron Spectrosc.* **108**, 13 (2000), K. Suzuki, S. Ishiuchi and M. Fujii, *Faraday Discuss.* **115**, 229 (2000), K. Sakota, N. Yamamoto, K. Ohashi, H. Sekiya, M. Saeki, S. Ishiuchi, M. Sakai and M. Fujii, *Chem. Phys. Lett.* **341**, 70 (2001).
- 5) S. Ishiuchi, M. Saeki, M. Sakai and M. Fujii, *Chem. Phys. Lett.* **322**, 27 (2000).
- 6) M. Saeki, S. Ishiuchi, M. Sakai and M. Fujii, *J. Phys. Chem. A* **105**, 10045 (2001).
- 7) M. Sakai, K. Daigoku, S. Ishiuchi, M. Saeki, K. Hashimoto and M. Fujii, *J. Phys. Chem. A* **105**, 8651 (2001).
- 8) H. Yokoyama, H. Watanabe, T. Omi, S. Ishiuchi and M. Fujii, *J. Phys. Chem. A* **105**, 9366 (2001).
- 9) S. Ishiuchi, M. Sakai, K. Daigoku, T. Ueda, T. Yamanaka, K. Hashimoto and M. Fujii, *Chem. Phys. Lett.* **347**, 87 (2001).

III-E-1 Hydrogen Transfer in Photo-Excited Phenol/Ammonia Clusters by UV-IR-UV Ion Dip Spectroscopy and Ab Initio MO Calculations I: Electronic Transitions

(¹Tokyo Metropolitan Univ./ACT-JST)

[*J. Chem. Phys.* in press]

ISHIUCHI, Shun-ichi; DAIGOKU, Kota¹; SAEKI, Morihisa; SAKAI, Makoto; HASHIMOTO, Kenro¹; FUJII, Masaaki

(¹Tokyo Metropolitan Univ./ACT-JST)

[*J. Chem. Phys.* in press]

The electronic spectra of reaction products via photo-excited phenol / ammonia clusters (1:2~5) have been measured by UV-near-IR-UV ion dip spectroscopy. Compared with the electronic spectra of hydrogenated ammonia cluster radicals the reaction products have been proven to be $(\text{NH}_3)_{n-1}\text{NH}_4$ ($n = 2 \sim 5$), which are generated by excited-state hydrogen transfer in $\text{PhOH-(NH}_3)_n$. By comparing the experimental results with *ab initio* molecular orbital calculations at multi-reference single and double excitation CI level, it has been found that the reaction products, $(\text{NH}_3)_{n-1}\text{NH}_4$ (for $n = 3$ and 4), contain some isomers.

III-E-2 Hydrogen Transfer in Photo-Excited Phenol/Ammonia Clusters by UV-IR-UV Ion Dip Spectroscopy and Ab Initio MO Calculations II: Vibrational Transitions

ISHIUCHI, Shun-ichi; DAIGOKU, Kota¹; SAEKI, Morihisa; SAKAI, Makoto; HASHIMOTO, Kenro¹; FUJII, Masaaki

The vibrational spectra of phenol/ammonia clusters (1:2 ~ 5) in S_0 and those of their photo chemical reaction products, $(\text{NH}_3)_{n-1}\text{NH}_4$ ($n = 2 \sim 5$), which are generated by excited-state hydrogen transfer, have been measured by UV-IR-UV ion dip spectroscopy. The geometries, IR spectra and normal modes of phenol- $(\text{NH}_3)_n$ ($n = 1 \sim 5$) have been examined by *ab initio* molecular orbital calculations, at the second-order Møller-Plesset perturbation theory level with large basis sets. For the $n = 2$ and 3 reaction products, similar vibrational analyses have been carried out. From the geometrical information of reactants and products, it has been suggested that the reaction products have memories of the reactant's structure, which we call "memory effect."

III-E-3 Picosecond Time-Resolved Infrared Spectra of Photo-Excited Phenol-(NH₃)₃ Cluster

ISHIUCHI, Shun-ichi; SAKAI, Makoto; DAIGOKU, Kota¹; UEDA, Tadashi; YAMANAKA, Takaya; HASHIMOTO, Kenro¹; FUJII, Masaaki

(¹Tokyo Metropolitan Univ./ACT-JST)

[*Chem. Phys. Lett.* **347**, 87 (2001)]

Picosecond time-resolved IR spectra of phenol- $(\text{NH}_3)_3$ have been measured by UV-IR-UV ion dip spectroscopy for the first time. It was found that the

time-evolution of two vibrational bands at 3180 cm^{-1} and 3250 cm^{-1} is different from each other. The results show that two transient species are generated from the photo-excited phenol-(NH_3)₃ cluster. From *ab initio* calculation, the transient species are assigned to two isomers of (NH_3)₂NH₄.

III-E-4 Picosecond Time-Resolved Nonresonant Ionization Detected IR Spectroscopy on 7-Azaindole Dimer

SAKAI, Makoto; ISHIUCHI, Shun-ichi; FUJII, Masaaki

[*Eur. Phys. J. D* in press]

The picosecond time-resolved IR spectrum of the 7-azaindole dimer has been measured by picosecond time-resolved nonresonant ionization detected IR spectroscopy. This new time-resolved technique was developed by combining nonresonant ionization detected IR (NID-IR) spectroscopy with tunable picosecond IR and UV lasers. The time-resolved NID-IR spectrum from 2600 cm^{-1} to 3800 cm^{-1} shows a drastic change from 1.5 ps to 11 ps time evolution. A mode-specific vibrational redistribution has been suggested.

III-E-5 Structure of Hydrogen-Bonded Clusters of 7-Azaindole Studied by IR Dip Spectroscopy and Ab Initio Molecular Orbital Calculation

YOKOYAMA, Hiroshi¹; WATANABE, Hidekazu²; OMI, Takuichiro¹; ISHIUCHI, Shun-ichi; FUJII, Masaaki
(¹Waseda Univ./PRESTO; ²AIST)

[*J. Phys. Chem. A* **105**, 9366 (2001)]

The IR spectrum of 7-azaindole monomer, 7-azaindole reactive and nonreactive dimers, and 7-azaindole (H_2O)_{*n*} (*n* = 1–3) clusters in a supersonic jet from 2600 cm^{-1} to 3800 cm^{-1} have been measured using IR dip spectroscopy. The vibrational transitions in the ground state were clearly observed and were assigned to the CH and NH stretching vibrations of 7-azaindole and the OH stretching vibrations of water molecules in the clusters. The observed IR spectra of 7-azaindole monomer and 7-azaindole(H_2O)_{*n*} (*n* = 1–3) clusters were compared to theoretical ones obtained by *ab initio* MO calculations. From a comparison, it is concluded that 7-azaindole-(H_2O)_{*n*} (*n* = 1–3) clusters have a ring structure due to a cyclic hydrogen-bond network. This conclusion is consistent with an analysis based on high-resolution spectroscopy. Similarly, the IR dip spectrum suggests that the 7-Azaindole reactive dimer has a cyclic hydrogen-bond network, forming a symmetric planer structure. It is strongly suggested from the IR spectrum and the *ab initio* calculations that the nonreactive dimer contains a water molecule between 7-azaindole molecules.

III-E-6 Structures of Carbazole-(H_2O)_{*n*} (*n* = 1–3) Clusters Studied by IR Dip Spectroscopy and a Quantum Chemical Calculation

SAKAI, Makoto; DAIGOKU, Kota¹; ISHIUCHI, Shun-Ichi; SAEKI, Morihisa; HASHIMOTO, Kenro¹; FUJII, Masaaki
(¹Tokyo Metropolitan Univ./ACT-JST)

[*J. Phys. Chem. A* **105**, 8651 (2001)]

The IR spectra of carbazole and carbazole-(H_2O)_{*n*} (*n* = 1–3) clusters in a supersonic jet have been measured by IR dip spectroscopy. The spectra show clear vibrational structures of both the monomer and the clusters in the 2900–3800 cm^{-1} frequency region. The observed vibrational bands are assigned to the NH stretch of carbazole and the OH stretches of H_2O molecules in the clusters. The geometries and IR spectra of carbazole-(H_2O)_{*n*} clusters were calculated at the HF/6-31G and B3LYP/6-31++G(d,p) levels. From a comparison of the observed and calculated IR spectra, the structures of the cluster have been determined.

III-E-7 Structure of 1-Naphthol/Alcohol Clusters Studied by IR Dip Spectroscopy and Ab Initio Molecular Orbital Calculations

SAEKI, Morihisa; ISHIUCHI, Shun-Ichi; SAKAI, Makoto; FUJII, Masaaki

[*J. Phys. Chem. A* **105**, 10045 (2001)]

The structures of 1-naphthol/alcohol clusters, 1-NpOH(ROH)_{*n*} (*n* = 1–3; ROH = MeOH, EtOH, and *t*-BuOH), have been investigated by resonant two-photon ionization (R2PI) spectroscopy and ion-detected IR dip spectroscopy. Based on the calculated spectra obtained by *ab initio* MO calculations, the spectra of 1-NpOH-(MeOH)_{*n*} was analyzed. The analysis elucidated that 1-NpOH(MeOH)_{2,3} was a ring structure. From a similarity of the spectral pattern, the structures of 1-NpOH(EtOH)_{*n*} and 1-NpOH(*t*-BuOH)_{*n*} were also determined to be a ring conformation. From a frequency shift of the hydrogen-bonded OH stretching vibration, the hydrogen bonding is weakened by a steric hindrance due to an alkyl group of ROH. The difference in the solvation mechanism between 1-NpOH(MeOH)_{*n*} and 1-NpOH-(H_2O)_{*n*} is discussed.

III-E-8 Pulsed Field Ionization Zero Kinetic Energy Photoelectron Study on Methylanisole Molecules in a Supersonic Jet

KINOSHITA, Shin-ichi¹; KOJIMA, Hiroshi¹; SUZUKI, Tadashi¹; ICHIMURA, Tejiro¹; YOSHIDA, Keigo; SAKAI, Makoto; FUJII, Masaaki
(¹Tokyo Inst. Tech.)

[*Phys. Chem. Chem. Phys.* **3**, 4889 (2001)]

Pulsed-field ionization zero kinetic energy (PFI-ZEKE) photoelectron spectra were measured for jet-cooled *o*-, *m*-, and *p*-methylanisoles for the first time. The low-frequency bands observed at around the origin band in the spectra were assigned to the methyl internal rotational bands of the cations. The potential curves and the Franck-Condon factors for the methyl internal rota-

tional motion were calculated by the one-dimensional free-rotor approximation. The potential barrier height was found to change drastically on ionization, suggesting that the electronic structure should mainly affect the potential barrier of the methyl internal rotation.

tion. The spectroscopic and theoretical results are in agreement with a relatively weak intramolecular hydrogen bond.

III-E-9 The PFI-ZEKE Photoelectron Spectrum of *m*-Fluorophenol and its Aqueous Complexes: Comparing Intermolecular Vibrations in Rotational Isomers

YOSHIDA, Keigo; SUZUKI, Kazunari; ISHIUCHI, Shun-ichi; SAKAI, Makoto; FUJII, Masaaki; DESSENT, Caroline E. H.¹; MÜLLER-DETHLEFS, Klaus¹

(¹Univ. York, UK)

[*Phys. Chem. Chem. Phys.* **4**, 2534 (2002)]

Pulsed Field Ionization–Zero Kinetic Energy (PFI-ZEKE) Photoelectron spectroscopy has been applied to study the cationic ground states of the rotational isomers of *m*-fluorophenol and its hydrogen-bonded clusters with H₂O and D₂O. The *cis*- and *trans*- monomer isomers are assigned by comparing the observed ionization potentials with values obtained from *ab initio* calculations (HF/6-31G*). Both monomers display very similar vibrational frequencies, indicating that the geometric structures of the two cations are similar. In contrast, the *cis*- and *trans*-aqueous clusters display distinctive intermolecular vibrational frequencies (*e.g.* the intermolecular stretching vibrations appear at 239 and 228 cm⁻¹ in the *cis*- and *trans*-isomers respectively). The origin of the different intermolecular interactions in the isomeric clusters is discussed with reference to the *ab initio* calculations.

III-E-10 OH- and CH-Stretching Overtone Spectra of Catechol

KJAERGAARD, Henrik G.¹; HOWARD, Daryl L.¹; SCHOFIELD, Daniel P.¹; ROBINSON, Timothy W.¹; ISHIUCHI, Shun-ichi; FUJII, Masaaki

(¹Univ. Otago, New Zealand)

[*J. Phys. Chem. A* **106**, 258 (2002)]

We have recorded the CH-, OH-, and OD-stretching fundamental and overtone spectra of catechol (1,2-dihydroxybenzene, pyrocatechol) and selectively deuterated catechol. Conventional and intracavity photoacoustic spectroscopy were used to record room temperature spectra of catechol in solution and in the vapor phase, whereas nonresonant ionization detected spectroscopy was used to study catechol in a supersonic jet. The spectra can be explained in terms of a local mode model with one oscillator for each of the non-equivalent CH, OH, or OD bonds. Intensities of the CH-, OH-, and OD-stretching transitions were calculated with an anharmonic oscillator local mode model and *ab initio* determined dipole moment functions. Our simple calculations are in good agreement with the observed intensities. Line widths in the jet-cooled spectra are discussed in terms of intramolecular vibrational redistri-

III-F Ultrafast Molecular Dynamics Studied by Time-Resolved Photoelectron Imaging

Femtosecond pump-probe time-resolved photoelectron imaging is a novel experimental approach to probe electronic and nuclear dynamics in real time. Since photoionization can occur from any part of the potential energy surfaces with any multiplicity, the method provides a versatile means to follow dephasing and reaction processes.

III-F-1 Ionization Dynamics of NO A ($2\Sigma^+$) State Studied by Time-Resolved Photoelectron Imaging

TSUBOUCHI, Masaaki¹; SUZUKI, Toshinori
(¹GUAS)

Photoionization dynamics of NO from the $A^2\Sigma^+$ ($3s\sigma$ Rydberg) state is studied by femtosecond photoelectron imaging method. The photoelectron angular distribution (PAD) observed in the laboratory frame (LF) is convolution of the PAD in the molecular frame (MF) with the molecular axis distribution in space. Our method utilizes a rotational wavepacket created by coherent excitation of the molecular ensemble to control the axis distribution, and the LF-PAD is measured as a function of this distribution. Then, the LF-PAD is deconvoluted with the axis distribution to obtain the MF-PAD. The PADs in (1+1') REMPI *via* the A state are well expressed by expansion with the Legendre polynomials,

$$I(\theta; t) \propto 1 + \beta_2(t)P_2(\cos\theta) + \beta_4(t)P_4(\cos\theta).$$

Figure 1 shows the time dependence of the expansion coefficients, β_L , observed for several probe wavelengths. All profiles exhibit modulation with 8.4 ps time period in agreement with the rotational constant of NO in the A state, $B = 1.997\text{ cm}^{-1}$. The phase of the modulation varies with the probe wavelength, clearly indicating that the ionization dynamics of NO from the A state is energy-dependent. The ionization dynamical parameters are extracted from the β_L parameters.

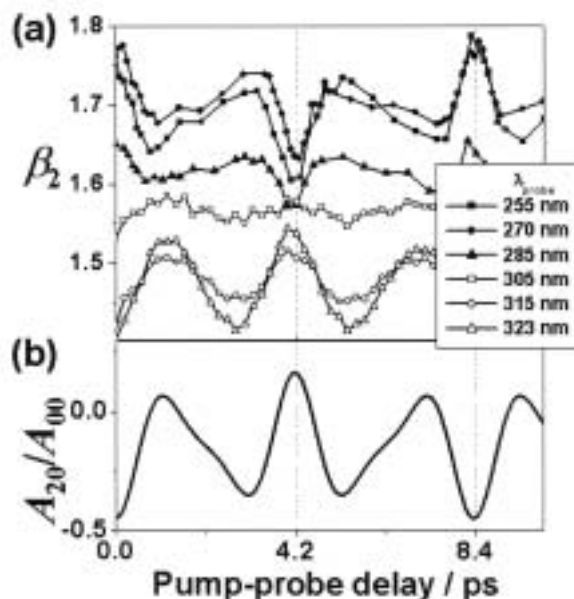


Figure 1. (a) Temporal profiles of the β_2 anisotropy parameter of LF-PADs observed by [1+1'] femtosecond photoelectron imaging with several probe wavelengths. (b) Calculated time evolution of the alignment parameter, A_{20}/A_{00} , for the molecular axis distribution,

$$P(\theta, \phi) = A_{00}Y_{00}(\theta, \phi) + A_{20}Y_{20}(\theta, \phi),$$

on the optically excited NO A state.

III-F-2 Theoretical Analysis of Rotational Revivals in Intersystem Crossing in Pyrazine

TSUBOUCHI, Masaaki¹; WHITAKER, Benjamin J.²; SUZUKI, Toshinori
(¹GUAS; ²Leeds Univ.)

In our previous work, we have visualized the decay of the S_1 and the buildup of the T_1 state in the $S_1(n, \pi^*) \rightarrow T_1(n, \pi^*)$ intersystem crossing (ISC) of pyrazine using the (1+2') femtosecond photoelectron imaging.^{1,2} A rotational wavepacket motion created by coherent excitation of multiple rovibrational states in the S_1 state was clearly observed in the temporal behavior of photoelectron intensities. The signature of the rotational wavepacket motion is also seen in the T_1 state, however, this amplitude was much smaller than the one observed for the S_1 state. We attempted theoretical analysis of this phenomenon. A model Hamiltonian matrix for a singlet state and multiple triplet states is diagonalized to form molecular eigenstates, and coherent excitation of these ensemble states is considered. The spin-orbit coupling strength and the density of triplet states are assumed to reproduce the observed dephasing time. The time-dependent alignment in the S_1 and T_1 states are calculated. Figure 1 shows the experimental and calculated time evolutions of the alignment parameter, A_{20}/A_{00} , for the molecular axis distribution,

$$P(\theta, \phi) = A_{00}Y_{00}(\theta, \phi) + A_{20}Y_{20}(\theta, \phi).$$

The rotational quantum beats in the singlet and triplet signals are reproduced well, where the model correctly predicts weaker alignment for the triplet states.

References

- 1) T. Suzuki *et al.*, *J. Chem. Phys.* **111**, 4859 (1999).
- 2) Tsubouchi *et al.*, *Phys. Rev. Lett.* **115**, 8810 (2001).

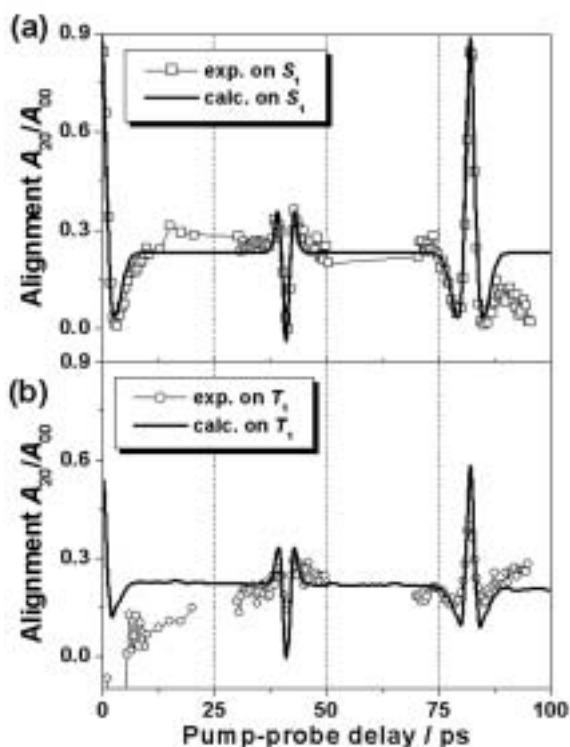


Figure 1. Time evolutions of the alignment parameter, A_{20}/A_{00} , for the molecular axis distribution,

$$P(\theta, \phi) = A_{00}Y_{00}(\theta, \phi) + A_{20}Y_{20}(\theta, \phi),$$

on (a) the S_1 and (b) the T_1 state. Square (\square) and circle (\circ) represent the experimentally determined alignment parameter which derived from the time profiles of the photoionization partial cross section from the S_1 and the T_1 state, respectively. Solid lines are simulation profiles taking into account the rotational wavepacket motion.

III-F-3 Femtosecond Photoelectron Imaging on Pyridazine: S_1 Decay Rate and $3s$ and $3p$ Rydberg State Energetics

**KIM, Sang Kyu¹; MATSUMOTO, Yoshiteru;
SUZUKI, Toshinori**
(¹Inha Univ., Korea)

Diazabenzenes have received extensive experimental and theoretical studies as the benchmark systems for investigation of electronic dephasing processes. In particular, pyrazine is the best-studied molecule of an intermediate case and it is well accepted now that the optically prepared S_1 pyrazine dephases into the T_1 manifold with a lifetime of 110 ps. Our previous study on pyrazine by time-resolved photoelectron imaging has firmly established this dynamics by visualizing both the decay of the S_1 and the buildup of T_1 characters in real time.¹⁾⁻³⁾ Comparing with pyrazine and pyrimidine, pyridazine is the least-studied member of diazabenzene. There seem to be still debates on various fundamental properties of excited state such as the S_1 lifetime, spectral assignment of S_1 origin, and energetics of low-lying Rydberg states. Another interesting issue is that although pyrazine dephases mainly to the triplet manifold, it has been suggested that pyridazine dephases down to the ground electronic state. We have performed the first time-resolved study on the excited states of pyridazine by femtosecond photoelectron imaging. The lifetime of the S_1 state is 340 ps at the origin and decreases at higher vibrational energies, and no clear signature of the triplet states was observed. The $3s$ (n^{-1}) and $3p$ (n^{-1}) Rydberg states of pyridazine are identified in angle- and energy-resolved photoelectron images obtained by the $(1+2')$ excitation where these Rydberg states act as intermediate resonant states in photoionization process, providing respective term values of 5.67 and 6.27 eV.

References

- 1) T. Suzuki *et al.*, *J. Chem. Phys.* **111**, 4859 (1999).
- 2) Tsubouchi *et al.*, *Phys. Rev. Lett.* **115**, 8810 (2001).
- 3) Song *et al.*, *J. Chem. Phys.* **86**, 4500 (2001).

III-G Non-Adiabatic Photodissociation Dynamics of Fundamental Molecules

Detailed investigation on photodissociation dynamics of fundamental molecules is extremely important not only for elucidating chemical reaction mechanisms but also for accurate modeling of atmospheric chemistry. Hyperthermal kinetic energy distribution of reaction products, hot band contribution in photoabsorption, and non-adiabatic dynamics are important for understanding isotope fractionation, branching ratios in bimolecular reactions *etc.* in the atmosphere.

III-G-1 Non-Adiabatic Bending Dissociation of OCS: The Effect of Bending Excitation on the Transition Probability

KATAYANAGI, Hideki; SUZUKI, Toshinori

[*Chem. Phys. Lett.* **360**, 104 (2002)]

In our previous work, an interesting non-adiabatic

dissociation mechanism of OCS induced by fast bending motion in the electronically excited state has been discovered.¹⁾ In the present work, UV photodissociation dynamics of OCS starting from the bending excited (010) state was compared to that from the ground vibrational state (000). The rotational distribution of $\text{CO}(X^1\Sigma^+)$ was measured by (2+1) resonance enhanced multiphoton ionization, in which dissociations from the two different initial states were discriminated from the

translational energies of the CO fragments. Quantitative analysis revealed that the non-adiabatic transition probability in dissociation starting from (010) was 0.21 that is similar to but slightly smaller than the value, 0.34, from (000).

Reference

1) Suzuki *et al.*, *J. Chem. Phys.* **109**, 5778 (1998).

III-G-2 Velocity Map Fragment Imaging on 205 nm Photodissociation of Nitrous Oxide

KATAYANAGI, Hideki; NISHIDE, Tatsuhiro;
SUZUKI, Toshinori

Photodissociation of N₂O at 205 nm is reexamined by the velocity map ion imaging of N₂ and O(¹D₂) fragments. The kinetic energy distribution of the O atoms measured by using (2+1) REMPI via the ¹P₁ state is in excellent agreement with the one reported previously by

a conventional imaging method without two-dimensional space focusing.¹⁾ The angular distribution of the O atoms is expressed by expansion with up to the 6-th order Legendre polynomial, indicating the orbital alignment as reported previously.¹⁾ A bell-shaped rotational distribution of N₂ is observed, where its width is somewhat narrower than previous observations. From the rotational distribution of N₂ due to photoexcitation from the (000) and (010) states of N₂O and the ion image of state-selected N₂, the magnitude of the transition strengths from the (000) and (010) levels were estimated. The angular anisotropy of N₂ fragments is in excellent agreement with the results by Neyer *et al.*²⁾ Rather low angular anisotropy, $\beta < 1.0$, indicates that photoabsorption to the A''(¹Σ⁻) state is not negligible at 205 nm.

References

1) Suzuki *et al.*, *Chem. Phys. Lett.* **256**, 90 (1996).

2) Neyer *et al.*, *J. Phys. Chem. A* **103**, 10388 (1999).

III-H Development of New Devices for Molecular Dynamics Experiments

III-H-1 Three Dimensional Photofragment Imaging Using a Fast Response Imager

SUZUKI, Toshinori; KATAYANAGI, Hideki

An inverse Abel transform is often used for reconstructing a 3D object from its 2D projection, when the original distribution is cylindrically symmetric. In pump and probe experiments, this condition is fulfilled only when the polarization directions of the two beams are aligned parallel to each other. For investigating vector correlation in photodissociation, it is useful to use cross polarization of two laser beams, which inevitably destroys the cylindrical symmetry required for an inverse Abel transform. For obtaining the 3D scattering distribution for cross polarization, time and position sensitive detection methods must be employed. Currently, a delay line anode imaging device is widely used for the time and position sensitive detection of particles. However, this method is able to receive particles only less than 10 in a given response time, about 10 ns, and it is not ideal for the experiments with low repetition lasers, where tens of particles are detected within 10 ns. We use a dual microchannel plate backed by a plastic scintillator with an emission life time of about 3 ns and capture a transient image on this screen with a gated camera with a time-resolution of 3 ns. Several designs for the acceleration electrodes were carefully tested.

III-H-2 High Repetition Rate Two Dimensional Imaging Using C-MOS Imager

SUZUKI, Toshinori; TSUBOUCHI, Masaaki

The imaging experiment suffers from non-uniform

sensitivity of an imaging system over the area. This originates from an unavoidable pulse height (brightness) distribution of an MCP with a phosphor screen, and the most effective method to correct it is to perform real-time image processing on each image due to a single laser shot. Previously, we have performed real-time thresholding and centroiding calculations for measurements with 25 Hz system rate, while it is no longer applicable to experiments run at 1 kHz since it is by far higher rate of a regular video rate, 25 Hz. In collaboration with HAMAMATSU Co. Ltd., a 1 kHz C-MOS camera system with a real-time image processing was constructed and tested by performing 2D real-time electron counting with a 1 kHz Ti:sapphire femtosecond laser.

III-H-3 Construction of a Rotating-Source Crossed Beam Apparatus

KOYGUCHI, Hiroshi; SUZUKI, Toshinori

A new crossed beam apparatus with a rotating source has been designed for reactive scattering experiments on the O(¹D₂) reactions. The crossing angle can be varied from 30 to 180 degrees for continuously changing the collision energies. The O(¹D₂) atoms are generated by photolysis of O₂ molecules at 157 nm produced by a F₂ laser.

III-I Structure and Properties of Polyoxometalates with a Magnetic, Electronic, or Biological Significance

Polyoxometalates constitute model systems for the study of the electron and energy transfer in the infinite metal-oxide lattice and their simplicity allows to treat at the molecular scale the coupling of electronic and nuclear movements, which is an inherent problem for the mixed-valence systems. As is clear from such a variety of both structure and reactivity of polyoxometalates, our current works on polyoxometalates are 1) structure/reactivity relationships with particular regard to the mechanism of electron transfer reactions, 2) magnetic interaction and molecular magnetic device, 3) energy-transfer mechanism and luminescence device (including nonlinear optical device), 4) encapsulation of templates in the photo-induced self-assembly process, 5) template-exchange reaction and topology, and 6) antibacterial effects on methicillin-resistant *Staphylococcus aureus* (MRSA) and human gastric pathogen of *Helicobacter pylori*.

III-I-1 Synthesis and Crystal Structure of a Novel Vanadium-Containing Tungstobismutate(III)K₁₂[(VO)₃(BiW₉O₃₃)₂]-30H₂O

BOTAR, Bogdan¹; YAMASE, Toshihiro²;
ISHIKAWA, Eri¹
(¹Tokyo Inst. Tech.; ²IMS and Tokyo Inst. Tech.)

[*Inorg. Chem. Commun.* **4**, 551 (2001)]

The tris(vanadyl)-substituted tungstobismutate(III) [(VO)₃(BiW₉O₃₃)₂]¹²⁻ anion has been synthesized by reaction of α -B[BiW₉O₃₃]⁹⁻ with VOSO₄ in aqueous solution. The anion is made of two α -B[BiW₉O₃₃]⁹⁻ unit linked by a belt of three exterior VO²⁺ groups into an assembly of virtual D_{3h} symmetry. The three vanadium centers are well separated by V...V distance of 5.375(4)–5.474(4) Å.

III-I-2 Crystallization and Structural Characterization of Two Europium Molybdates, Eu₄Mo₇O₂₇ and Eu₆Mo₁₀O₃₉

NARUKE, Haruo¹; YAMASE, Toshihiro²
(¹Tokyo Inst. Tech.; ²IMS and Tokyo Inst. Tech.)

[*J. Solid State Chem.* **161**, 85 (2000)]

Crystals of two new europium molybdates, Eu₄Mo₇O₂₇ and Eu₆Mo₁₀O₃₉, were grown in a melt of Eu₂O₃·6.1–6.5MoO₃ obtained by thermal decomposition of [Eu₂(H₂O)₁₂Mo₈O₂₇]·6H₂O or firing of the Eu₂O₃ + 8MoO₃ mixture at 800 °C for 2 h in air. Repeated uses of reaction containers are effective in the crystallization. Eu₄Mo₇O₂₇ crystallized in monoclinic, C2/c (No. 15), $a = 23.031(1)$, $b = 14.720(1)$, $c = 14.4097(7)$ Å, $\beta = 105.174(2)^\circ$, $V = 4714.8(4)$ Å³, $Z = 8$, $R_1 = 0.035$, and $wR_2 = 0.064$. Eu₄Mo₇O₂₇ is a layer compound consisting of {MoO₄}- and {Mo₃O₁₁}-containing layers parallel to the bc plane and interstitial Eu atoms. Eu₆Mo₁₀O₃₉ crystallized in monoclinic, C2/c (No. 15), $a = 12.3008(5)$, $b = 19.6596(9)$, $c = 13.7691(47)$ Å, $\beta = 100.8934(9)^\circ$, $V = 3269.8(2)$ Å³, $Z = 4$, $R_1 = 0.036$, and $wR_2 = 0.101$. The structure of Eu₆Mo₁₀O₃₉ is constructed of three-dimensionally arranged {MoO₄} and {Mo₂O₇} groups and Eu atoms, being closely related to the structure of Ce₆Mo₁₀O₃₉. In both compounds, Eu

atoms achieve seven- or eight-fold coordination by O atoms (< 2.7 Å), and two EuO_{*n*} polyhedra share their edges or faces with a short Eu...Eu separation ranging from 3.6297(8) to 3.7168(6) Å.

III-I-3 Nanocluster Crystals of Lacunary Polyoxometalates as Structure-Design-Flexible, Inorganic Nonlinear Materials

MURAKAMI, Hidetoshi; KOZEKI, Toshimasa;
SUZUKI, Yuji; ONO, Shingo; OHTAKE, Hideyuki;
SARUKURA, Nobuhiko; ISHIKAWA, Eri¹;
YAMASE, Toshihiro²
(¹Tokyo Inst. Tech.; ²IMS and Tokyo Inst. Tech.)

[*Appl. Phys. Lett.* **79**, 3564 (2001)]

Lacunary polyoxometalates, large inorganic, structure-design-flexible, nanocluster crystals are found to have optical nonlinearity than KH₂PO₄ by the powder second-harmonic-generation method. Moreover, the capability of generating ultraviolet radiation down to around 300 nm is found. The basic criteria to design the high nonlinearity are also discovered by the reduction of the molecular symmetry.

III-I-4 A Three-Dimensional Inorganic/Organic Hybrid Vanadium Oxide Complex with Pentacoordinate Co^{II}, [CoV₂O₆(4,4'-bipy)]

YANG, Lan¹; NARUKE, Haruo¹; YAMASE, Toshihiro²
(¹Tokyo Inst. Tech.; ²IMS and Tokyo Inst. Tech.)

[*Acta Crystallogr., Sect C: Cryst. Struct. Commun.* **57**, 1378 (2001)]

The title compound, poly{[cobalt(II)- μ -(hexaaxodivandium-*O*:*O'*)]- μ -bipyridine-N:N'}, [CoV₂O₆(C₁₀H₈N₂)], has been prepared hydrothermally and characterized by elemental analyses, IR spectroscopy and single-crystal X-ray diffraction. The structure consists of bimetallic oxide layers, [Co₂V₄O₁₂], linked through 4,4'-bipyridine ligands into a three-dimensional network.

III-I-5 Tb₂Mo₄O₁₅

NARUKE, Haruo¹; YAMASE, Toshihiro²
(¹Tokyo Inst. Tech.; ²IMS and Tokyo Inst. Tech.)

[*Acta Crystallogr., Sect E* **57**, 1106 (2001)]

The title compound, tetramolybdenum(VI) diterbate (III), was prepared by pyrolysis of Tb₂(H₂O)₁₂Mo₈O₂₇·6H₂O at 1023 K for 2 h in air. The structure consists of trigonal bipyramidal MoO₅, tetrahedral MoO₄, and monocapped trigonal prismatic TbO₇ units. The two MoO₅ and two MoO₄ units are corner-shared, to form a Mo₄O₁₅ group.

III-I-6 H₂O₂-Based Epoxidation of Bridged Cyclic Alkenes with [P{Ti(O₂)₂W₁₀O₃₈}]⁷⁻ in Monophasic Systems: Active Site and Kinetics

GAO, Feixue¹; YAMASE, Toshihiro²; SUZUKI, Hideo¹
(¹Tokyo Inst. Tech.; ²IMS and Tokyo Inst. Tech.)

[*J. Mol. Catal. A* **180**, 97 (2002)]

The H₂O₂-based epoxidation of bridged cyclic alkenes in a monophasic system containing low concentrations (< 2 mM) of [Buⁿ₄N]₄[Pr₂NH₃]₂H[P{Ti(O₂)₂W₁₀O₃₈}]₂·H₂O (**1**) (with two η²-peroxotitanium sites in the anion) has been studied in search of the catalytically active species involved. ³¹P-NMR spectra of **1**, measured under a variety of conditions, revealed that the active species was not hydroperoxotitanium complex [P{Ti(OOH)}₂W₁₀O₃₈]⁷⁻ or [P{Ti(OOH)}Ti(O₂)W₁₀O₃₈]⁷⁻. The reaction pathways for the alkene epoxidation are discussed to understand the kinetics (especially the initial [H₂O₂] dependence). It was concluded that the net catalytic reaction for the epoxidation occurred through the two-electron oxidation at the hydroperoxotitanium site in the catalyst.

III-I-7 Photochemical Formation of a Lacunary Tire-Shaped Anion, [Mo₁₄₂O₄₃₂H₂₆(H₂O)₅₈]¹⁴⁻, through Degradative Self-Assembly of [Mo₃₆O₁₁₂(H₂O)₁₆]⁸⁻: Topology of Ring-Structural Molybdenum Blues

YAMASE, Toshihiro¹; PROKOP, Petra²
(¹IMS and Tokyo Inst. Tech.; ²Tokyo Inst. Tech.)

[*Angew. Chem. Int. Ed. Engl.* **41**, 466 (2002)]

A diamagnetic blue 28-electron reduced species [Mo^V₂₈Mo^{VI}₁₁₄O₄₃₂H₂₆(H₂O)₅₈]¹²⁻ ({Mo₁₄₂}) was produced photochemically through the degradative self-assembly of [Mo₃₆O₁₁₂(H₂O)₁₆]⁸⁻ ({Mo₃₆}). The molybdenum blue photochemistry favors not only the mechanistic investigation of the degradation self-assembly processes but also provides a basis for the molecular design of nano-sized ring clusters.

III-I-8 Size-dependent Population of Trivalent Rare Earth Cations (RE³⁺) in [(RE)₂(H₂O)₂(SbW₉O₃₃)(W₅O₁₈)₂]¹⁵⁻, and Structural Characterization of a Lutetium-Polyoxotungstate Complex [Lu₃(H₂O)₄(SbW₉O₃₃)₂(W₅O₁₈)₂]²¹⁻

NARUKE, Haruo¹; YAMASE, Toshihiro²
(¹Tokyo Inst. Tech.; ²IMS and Tokyo Inst. Tech.)

[*Bull. Chem. Soc. Jpn.* **75**, 12756 (2002)]

The effect of ionic radius of trivalent rare earth cations (RE³⁺) on the population at two square-antiprismatic sites (*Site I* and *Site II*) in [(RE)₂(H₂O)₂(SbW₉O₃₃)(W₅O₁₈)₂]¹⁵⁻ was studied by luminescence spectroscopic and X-ray crystallographic measurements in the Eu/Y- and Eu/Lu-mixed systems. The results indicated that a small RE³⁺ cation favorably occupies *Site II* where RE³⁺ is coordinated by four bridging O atoms of [SbW₉O₃₃]⁹⁻ and four terminal O atoms of [W₅O₁₈]⁶⁻. With the help of a structural characterization of pure [(RE)₂(H₂O)₂(SbW₉O₃₃)(W₅O₁₈)₂]¹⁵⁻ (RE = Er, Y, Dy, Eu, Sm), the large occupancy of small RE³⁺ at *Site II* was explained by a favorable coordination of [SbW₉O₃₃]⁹⁻ for small RE³⁺. A trial of the isostructural Lu complex unexpectedly showed formation of a novel [Lu₃(H₂O)₄(SbW₉O₃₃)₂(W₅O₁₈)₂]²¹⁻ complex which consists of two [Lu(SbW₉O₃₃)(W₅O₁₈)]¹²⁻ groups linked by [Lu(H₂O)₄]³⁺ with C₂ configuration.

III-I-9 Gd₄Mo₇O₂₇, a Novel Phase in the Gd₂O₃-MoO₃ System

NARUKE, Haruo¹; YAMASE, Toshihiro²
(¹Tokyo Inst. Tech.; ²IMS and Tokyo Inst. Tech.)

[*Acta Crystallogr., Sect E* **57**, i62 (2002)]

The title compound, heptamolybdenum(VI) tetragadolinate(III), a novel phase in the Gd₂O₃-MoO₃ system, has been prepared by pyrolysis of [Gd₂(H₂O)₁₂·Mo₈O₂₇]₂·6H₂O at 1023 K for 2 h in air. The compound can be described as a layer structure consisting of [MoO₄]-, [Mo₃O₁₁]-, and [Gds]-containing layers, which are stacked along the *a* direction. The coordination polyhedra of square-antiprismatic GdO₈ and monocapped trigonal prismatic GdO₇ are dimerized to give [Gd₂O_{*n*}] (*n* = 12 and 13) groups which possess short Gd···Gd separation [3.6345(4)–3.6404(4) Å].

III-I-10 Time-Resolved ESR-Spectroscopic Investigation of Polyoxometalate Photochemistry

YAMASE, Toshihiro
(IMS and Tokyo Inst. Tech.)

[*Catal. Catal.* **44**, 340 (2002)]

The time-resolved ESR spectroscopy is based on the detection of electron spin polarization (ESP) which let us enable to investigate the dynamics of the photochemically produced radicals. After a brief qualitative

and conceptual review of time-resolved ESR spectroscopy, exemplar photoredox reactions of polyoxometalates are discussed based on the observable chemically-induced-dynamic-electron -polarization (CIDEP) spectra which can be explained by the triplet mechanism.

III-J Electronic Spectroscopy and Excited-State Dynamics of Aromatics Clusters

Clusters are model systems for elucidating intermolecular interactions that control macroscopic properties of the molecules in condensed phases, such as liquids and crystals. We are investigating geometry and bonding topology of clusters containing aromatic molecules as well as their dynamical behavior after photoexcitation. This year we focus on detailed reexamination of electronic spectra of (benzene)_n clusters. Because benzene is a fundamental aromatic molecule with high symmetry, their aggregates have been subjected to vast numbers of experimental and theoretical studies for more than a quarter of a century. Still, there remain not a few issues under debate especially concerning to their electronic spectra. We succeeded in solving some of them by the present reexamination.

III-J-1 S₁–S₀ Vibronic Spectrum of the Benzene Tetramer

IIMORI, Toshifumi^{1,2}; OHSIMA, Yasuhiro³
(¹Kyoto Univ.; ²Nagoya Univ.; ³IMS and Kyoto Univ.)

[*J. Chem. Phys.* **117**, 3656 (2002)]

We reinvestigated the S₁–S₀ electronic transitions of (benzene)_n clusters by two-color mass-selective resonantly enhanced two-photon ionization (R2PI) and UV–UV hole burning spectroscopies. In this study, we explored the band system that has been assigned to the trimer for two decades. Hole burning measurements by monitoring the trimer ion isotopomer channels in the expansion of a mixture of C₆H₆ and C₆D₆ have shown the contribution of six spectral carriers in the R2PI spectra, two of which are isotopically pure clusters. The other hetero isotopic species containing at least one C₆H₆ moiety appear in two adjacent isotopomer channels. It is argued that the band system should be re-assigned to the neutral tetramer having four equivalent sites, which are detected in daughter ion mass channels due to efficient fragmentation after ionization even with two-color excitation. The experimental results are consistent with a distorted tetrahedral structure with S₄ symmetry predicted as the global minimum by several model calculations. This conclusion is further supported by an analysis of exciton splittings in the C₆H₆-localized origin band, and this analysis provides coupling constants for the excitation exchange in the S₁ state. Other experimental results reported so far pertaining to this species are reconsidered on the basis of the new assignment.

III-J-2 S₁–S₀ Vibronic Spectrum of the Benzene Trimer

IIMORI, Toshifumi^{1,2}; AOKI, Yasuhito¹;
OHSIMA, Yasuhiro³
(¹Kyoto Univ.; ²Nagoya Univ.; ³IMS and Kyoto Univ.)

[*J. Chem. Phys.* **117**, 3675 (2002)]

We further reexamined the S₁–S₀ transition of the (benzene)_n cluster that appears only in the dimer ion channel and thus has been assigned to an isomer of the neutral dimer other than the extensively studied T-shaped form. Mass-selective resonantly enhanced two-photon ionization (R2PI) excitation and UV–UV hole burning spectra are measured in the 0₀⁰ and 6₀⁰ vibronic regions. It is established from the observed spectra monitoring three isotopomer channels, (C₆H₆)₂⁺, [(C₆H₆)(C₆D₆)]⁺, and (C₆D₆)₂⁺, that efficient fragmentation following ionization prohibits one to observe the two-color R2PI spectra in the parent ion channels, similar to the case for the benzene tetramer as presented in III-J-1. Three neutral isotopomers containing at least one C₆H₆ moiety are identified, and this result argues the reassignment of the band system to the neutral benzene trimer with a cyclic form, where the three benzene sites are equivalent. The spectra of the homo isotopomers [(C₆H₆)₃ and (C₆D₆)₃] in the two vibronic regions exhibit small splittings due to the excitation exchange interactions, and this observation is discussed on the symmetry of the cluster geometry. Energetics pertaining to neutral and ionic benzene clusters are also discussed with previous experimental studies to assess a reason of the efficient fragmentation in the ionic states after R2PI for the trimer and larger clusters but not for the dimer.

III-K Electronic Spectroscopy of Molecules in Pendular States

When a molecule is subjected to a strong external electric field, pendular states are realized, where the electrostatic interaction by the field exceeds the molecular rotational energy and free rotation of the molecule changes to libration confined in the interaction potential. Thus, spectroscopic studies of pendular states will provide fundamental information toward establishing artificial manipulation of molecular orientation. We recently started investigation of electronic spectra of aromatic molecules in a strong DC electric field.

III-K-1 Construction of an Apparatus for Measurements of Fluorescence Excitation Spectra in a Strong DC Electric Field

KANYA, Reika¹; OHSHIMA, Yasuhiro²
(¹Kyoto Univ.; ²IMS and Kyoto Univ.)

We have recently constructed an experimental apparatus that enables measurements of fluorescence excitation spectra of molecules in a strong DC electric field. The apparatus is consisted of two differentially pumped vacuum chambers, as shown in Figure 1. A sample vapor diluted in He carrier gas is expanded through a heated pulsed nozzle, collimated by a conical skimmer, and passed through the center of two parallel electrodes in the second chamber. A linearly polarized light from a pulsed dye laser goes across the molecular beam in right angles, and the resultant fluorescence propagating to the downstream of the molecular beam is filtered and imaged onto a photomultiplier tube (PMT). The output of PMT is pre-amplified and fed into a boxcar. A combination of a Glan-laser polarizer and a variable wave plate is used to obtain highly polarized laser light with arbitrary orientation of linear polarization. The electrodes are so-called of Rogowski-type, which are designed to minimize the field inhomogeneity at their edges. By applying positive and negative high voltages to each of the electrodes, a uniform DC electric field up to 200 kV/cm can be achieved.

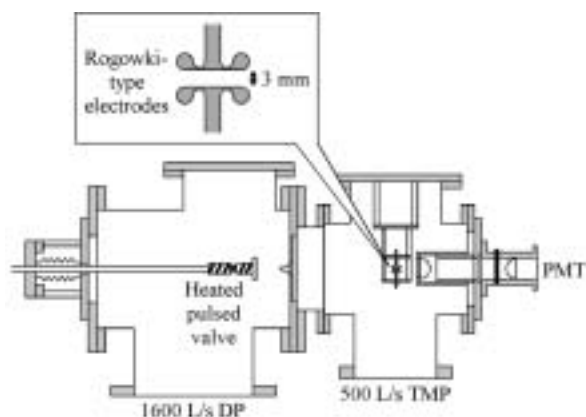


Figure 1. Schematic diagram of the experimental apparatus for measurements of fluorescence excitation spectra in a strong DC electric field. Close up of the Rogowski-type electrodes is shown as an inset.

III-K-2 Laser-Induced Fluorescence Spectra of Pendular-State Aromatics in a Strong DC Electric Field

KANYA, Reika¹; OHSHIMA, Yasuhiro²
(¹Kyoto Univ.; ²IMS and Kyoto Univ.)

With the experimental setup described in III-K-1, electronic transitions of several aromatic molecules like 9-cyanoanthracene (CNA) and *p*-aminobenzonitrile were observed under various DC electric field strengths. Figure 1 shows the S_1 - S_0 origin of CNA in the external electric field. The band contour changes drastically as the increase of the external field. In addition, altering polarization of the laser against the field provides an

entirely different shape in the spectra.

Because it is highly demanding computation to derive oscillator strength in a strong electric field for large asymmetric-top molecules like aromatics, some approximate method is indispensable. Considering that the interaction between the field and the molecular permanent dipole is dominant, we adopt a molecule-fixed axis system that is appropriate for the interaction. Then, the Hamiltonian is separated into zero-order terms that manifest pendular states for a symmetric top and remaining off-diagonal terms. Perturbation-theory treatments of the latter terms afford acceptably accurate calculations with greatly reduced computational time. Besides, we derived analytically, for the first time, energy levels and wavefunctions of a symmetric top in the pendular limit with corresponding quantum numbers.

Gross features of asymmetric-top pendular spectra are described in terms of the zero-order energy levels and selection rules. Indeed, the observed dependences for CNA on the electric field and the laser polarization are explained consistently, and its electric dipole moment is found to be increased by ~ 1.3 D after the $S_1 \leftarrow S_0$ excitation.

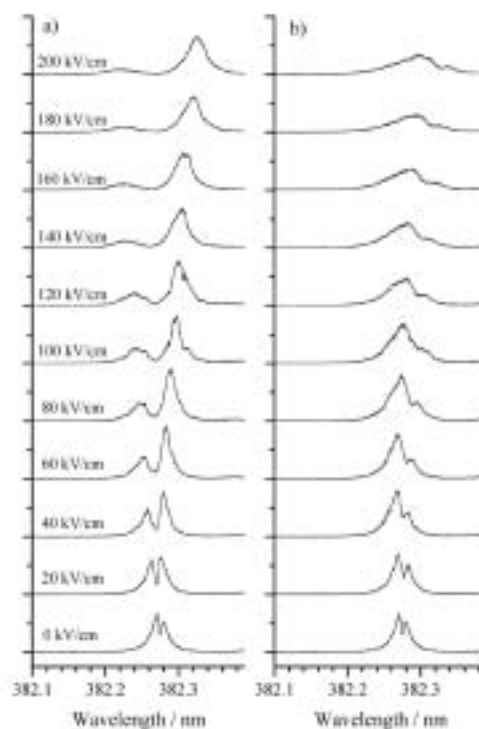


Figure 1. Electric field effects in LIF spectra of the S_1 - S_0 origin band of CNA. An angle between the laser polarization and the field is a) parallel, and b) perpendicular.

III-L Wave Packet Engineering Using a Phase-Programmable Femtosecond Optical Source

We proposed “wave packet engineering” which realizes mutual conversion between phase information of photonic and quantum wave packets by means of light-matter interaction. A phase-programmable femtosecond optical source is indispensable for such interactive control of photonic and quantum wave packets. We demonstrate control of quantum wave packets in organic molecules and semiconductors using phase-programmed pulses.

III-L-1 Single Molecular Phase-to-Amplitude Converter

MISAWA, Kazuhiko; MATSUDA, Isao¹; LANG, Roy¹

(¹Tokyo Univ. Agric. Tech., CREST(JST))

Control of quantum wave packets has been recently studied in various systems such as atoms, molecules, and semiconductors using chirp-controlled and phase-locked double pulses.¹⁾ In the present study, we observed wave-packet shaping by means of the phase-programmed femtosecond pulses in a cyanine dye molecule. The intra-pulse phase pattern of the pulses was converted to the amplitude of luminescence from the cyanine molecules.

The phase-programmable femtosecond optical source is composed of a femtosecond pulse oscillator, phase modulator and phase analyzer as shown in Figure 1. A femtosecond pulse with a spectral band width as broad as 160 nm is converted onto the Fourier plane. After a phase shift is provided to each spectral component with a spatial light modulator on the Fourier plane, the pulse is reconstructed. The output from the phase modulator is characterized by frequency resolved optical gating (FROG). The temporal profile and phase information of the femtosecond pulses can be obtained from the FROG measurement. A desired phase pattern can be realized through the iterative adjustment of the phase mask by analyzing the phase information. The center wavelength, pulse energy, duration, and phase-shift division of the source output were 802 nm, 0.64 nJ, 14 fs, and $6\pi/700$ radian, respectively. Figure 2 shows the spectra and phase dispersions for positively-chirped ($\Phi'' = 500$ fs²), transform-limited (0 fs²) and negatively-chirped pulses (-500 fs²).

Ethanol solution of a cyanine dye (IR-140) at a concentration of 4×10^{-4} M is circulated in a 0.5-mm thick quartz cell. The luminescence spectra of spontaneous emission are measured to evaluate the remaining excited-state population. Figure 3 shows the difference luminescence spectra of the positively-chirped (PC) and negatively-chirped (NC) excitations from the transform-limited excitation. The luminescence intensity is increased and decreased in case of PC and NC excitations, respectively. This chirp-dependent luminescence can be explained in terms of intra-pulse pump-dump process.²⁾ NC pulse induces narrow spatial distribution of the excited wave packet, while it is easily broadened and quickly escapes from the Franck-Condon window in PC case. The overlap integral between the excited- and ground-state wave packets determines the population, and as a result, the luminescence intensity.

In conclusion, we observed the remarkable dependence of luminescence intensity and the excited-state population in IR-140 molecules on the chirped pulse from the phase-programmable femtosecond optical source. The observed shaping of quantum wave packet opens a new possibility to process the intra-pulse phase information.

References

- 1) *Quantum Control of Molecular Reaction Dynamics*, R. J. Gordon and Y. Fujimura, Eds. (World Scientific, 2001).
- 2) K. Misawa and T. Kobayashi, *J. Chem. Phys.* **113**, 7546 (2000).

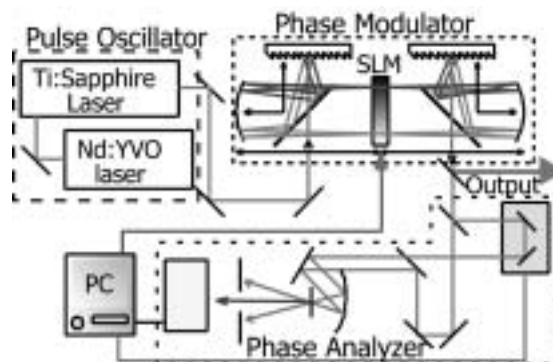


Figure 1. Schematic diagram of the phase-programmable femtosecond optical source.

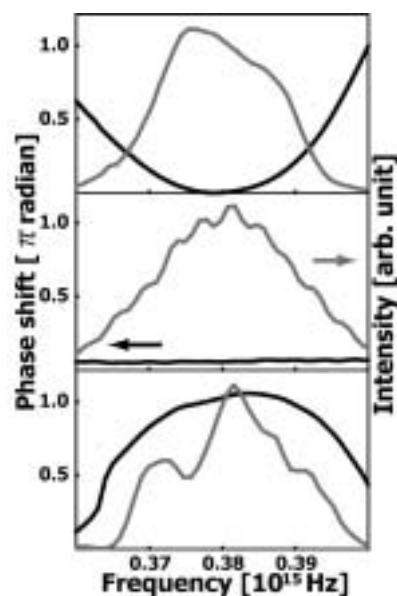


Figure 2. Spectra and phase dispersions of positively-chirped (top), transform-limited (middle) and negatively-chirped pulses (bottom).

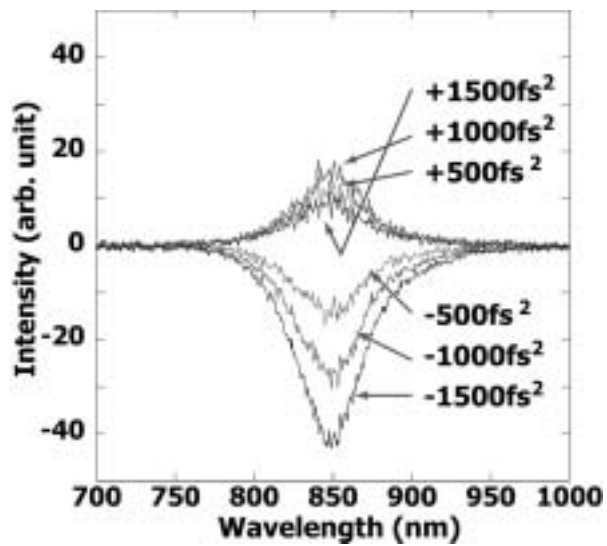


Figure 3. Difference luminescence spectra from IR-140 dye by the positively and negatively-chirped excitations with respect to the transform limited pulse.